AUT Journal of Electrical Engineering
10.22060/eej.2025.24075.5651

# Detection of Asymmetrical Short-Circuit Faults and Determination of the Faulty Line Section in Compensated Transmission Lines Equipped with Static Inter-phase Power Controller Based on Signal Processing Techniques

Mahyar Abasi [*1,2], Mostafa Yazdani Kachoei [3]

[1] Department of Electrical Engineering, Faculty of Engineering, Arak University, Arak 38156-8-8349, Iran.
[2] Research Institute of Renewable Energy, Arak University, Arak 38156-8-8349, Iran.
*m-abasi@araku.ac.ir
[3] Department of Electrical and ICT, Faculty of Technical Engineering, Institute for Higher Education, ACECR, Khouzestan, Iran.



**Abstract:**

The rapid advancements in power electronics and control systems have significantly contributed to the evolution of Flexible AC Transmission Systems, enabling the development of increasingly sophisticated compensation devices. Among these, the Static Inter-Phase Power Controller has emerged as a novel and extended configuration of the traditional Inter-Phase Controller, in which phase-shifting transformers are replaced by Static Synchronous Series Compensators, thereby offering enhanced controllability and operational flexibility. Despite its technical advantages, integrating Inter-Phase Power Controller into transmission networks introduces new protection challenges, particularly in accurately detecting fault locations due to the division of the line into two separate segments. This paper proposes a robust signal-processing-based method for detecting asymmetrical short-circuit faults and identifying the faulty line section in Static Inter-Phase Power Controller compensated transmission systems. The approach employs statistical indicators derived from the cumulative sum method and correlation coefficients among phase currents. By applying a heuristic comparison framework, the algorithm reliably detects fault occurrence and classifies the faulty segment with respect to the Inter-Phase Power Controller location. The proposed method is implemented in a MATLAB/Simulink environment and validated through extensive simulations covering 5,400 fault scenarios across various fault types, locations, and impedances. The results demonstrate an impressive accuracy rate of 98.46%, confirming the effectiveness and reliability of the algorithm under both nominal and stressed operating conditions.

AUT Journal of Electrical Engineering
10.22060/eej.2025.24075.5651

**Keywords:**

Asymmetrical short circuit, Correlation coefficient, Cumulative sum, Fault detection, SIPC.

## 1. Introduction

### 1-1- Research problem description

In recent years, the development of reactive power compensation devices based on voltage source converters has received considerable attention. Flexible AC Transmission Systems (FACTS) devices are regarded as prominent candidates for addressing various power system challenges due to their outstanding features. Issues related to power control and distribution, power quality improvement, operational enhancement, and system stability can be effectively addressed by optimal placement and utilization of FACTS devices. In the past few years, the development of these devices has increased their application [1, 2]. They have received much attention in the last few years due to their increased efficiency. One of the advanced devices from the FACTS family is the Static Inter-Phase Power Controller (SIPC) [3], which is an extension of the Inter-Phase Controller (IPC). In this new configuration, phase-shifting transformers are replaced with voltage source converters. The SIPC not only retains all the capabilities of the IPC but also introduces new features such as power flow control, active and reactive power range adjustment, fault current limitation, and voltage isolation [4]. Like the IPC, SIPC is installed in series within the transmission line. Although its presence in the network offers numerous advantages to the utility, it also introduces several challenges. One major challenge is related to line protection in systems where SIPC is installed. Typically located at the midpoint of the line, SIPC disrupts conventional distance protection schemes, making the design of specialized protection strategies a continuing research priority.

### 1-2- Challenges and necessity of the research

Traditional algorithms, such as the comprehensive distance protection scheme, face problems when a series compensator is placed in the transmission line, as transmission line parameters, including line impedance, change virtually. Fault detection, classification, and location become difficult, so there is a need to design

adaptive algorithms [1, 5]. On the other hand, considering that these devices divide the line into two parts, another challenge that arises is detecting the fault side relative to the compensator. In other words, when the SIPC is placed in the middle of a transmission line, the line is divided into two sections on the right and left from the perspective of a relay at one terminal (terminal 1). Given this division, the fault occurs either in the section between terminal 1 and SIPC or between terminal 2 and SIPC. A fundamental issue in protection designs is detecting the faulty side relative to SIPC. Most fault location algorithms depend on fault side detection relative to the compensator. Thus, the present study designs an algorithm for faulty section detection when an asymmetrical fault occurs in SIPC-compensated transmission lines. So far, various studies have been presented on fault occurrence detection and faulty section detection in the presence of series fault devices. However, each is related to specific studies of that device, and no study has ever focused on the problem of faulty section detection in SIPC-compensated transmission lines.

**1-3- A review of the literature**

A review of studies reveals that the protection algorithms in transmission lines have been designed for three main series compensators. The popular series compensators in transmission lines include series capacitors, thyristor-controlled series capacitors (TCSC), and static synchronous series compensators (SSSC). Based on this classification, the studies can be divided into three categories.

In reference [6], a new hybrid method based on wavelet transform and adaptive neuro-fuzzy inference system is proposed for faulty section identification, classification, and location in a series capacitor-compensated transmission line. The method extracts the characteristics of fault voltages and currents and uses them in a machine learning algorithm to specify the faulty section, type of fault, and location of the fault. In reference [7], a relaying pattern for directional relays in transmission lines equipped with a fixed series capacitor is presented through the incorporation of an artificial neural network. The base voltage and current signals are inputs to the neural network to identify the faulty section. Various parameters such as type of fault, fault location, fault incidence angle, and fault resistance are changed to examine the model. In reference [8], a relaying model based on the discrete wavelet transform is presented to detect and classify simultaneous single-phase-to-ground and open-circuit faults on a twelve-phase series capacitor-

compensated transmission line. In this study, the sensitivity analysis of the proposed method to variations in fault type, fault occurrence time, fault resistance, ground resistance, and fault location is tested and evaluated. Reference [9] introduces a new method to detect the fault type and faulty phase in a series capacitor-compensated transmission line. Standard deviation and discrete Stockwell transform are adopted along with a decision tree for fault classification. This method is used as a signal processing tool to extract the features of a half-cycle time window from the current and voltage signals sampled on one side of the network. Eventually, the standard deviation of the coefficients of the method after the fault is incorporated to form the input feature vector to a decision tree-based classifier. In reference [10], a combined method based on fuzzy logic and discrete Fourier transform is proposed for fault detection and classification in series capacitor-compensated transmission lines. In this method, the fundamental components of phase currents, phase voltages, and the zero-sequence current are applied as inputs to the model. Fault identification, fault phase selection, and fault classification are performed within half to one cycle of the fundamental frequency. In reference [11], a new method based on line current-voltage characteristics is developed to predict and recognize the location of faults and abnormal events in real time in a series capacitor-compensated transmission line. Once the currents and voltages of both sides of the line are measured, a single characteristic for the line is obtained. Any change in this characteristic can be identified and analyzed in real time using software in the control center. In this case, the location, type, and level of the unusual event or fault occurring can be identified.

In [12], an advanced fault location algorithm is proposed for three-terminal transmission lines connected to industrial microgrids. By utilizing phasor voltage and current data from PMUs, the algorithm determines the exact fault location without requiring fault type identification or line parameter estimation. This method is particularly well-suited for microgrid environments with renewable energy sources and bidirectional power flows. Similarly, [13] presents a novel analytical algorithm that uses asynchronous three-terminal voltage and current measurements to locate faults in series-compensated transmission lines, without the need for capacitor models or protection circuitry. The use of the Newton–Raphson method ensures high accuracy and robustness in fault location. Furthermore, [14] introduces a fast hybrid technique based on

Empirical Mode Decomposition (EMD) and Hilbert Transform, which detects faults by analyzing the energy of the dominant current mode. This approach can accurately detect faults in less than half a cycle and distinguish between fault and non-fault events. Collectively, these three studies reflect a clear trend toward fast, structure-independent, and practically robust fault detection and location algorithms suited to the complexities of modern power networks.

In reference [15], a method for classifying faults and specifying the location of faults in a TCSC-compensated transmission line is proposed using discrete wavelet transform. This method uses a cycle of current data with a sampling rate of 10 kHz. Also, the standard deviation of the eighth-level decomposition coefficient and the first-level decomposition coefficients are applied for fault classification and faulty section determination, respectively. In reference [16], the standard deviation and contour energy of the S-transform are used to help select the faulty phase and faulty section, and a method relying on the S-transform and probabilistic neural network (PNN) is proposed to classify faults in a TCSC-compensated transmission line. The features extracted by the S-transform are applied as the input of the PNN for fault classification. In reference [17], an improved method for fault analysis for the protection of TCSC-compensated transmission lines is presented. This method is a two-step method and uses half-cycle post-fault data for three current phases. In this reference, wavelet transform is adopted as a spectral analysis tool, and a neural network is utilized for classification. The method provides a significant improvement in the accuracy and speed of fault analysis for the protection of transmission lines with series compensation. In reference [18], an algorithm is presented for detecting, locating, and classifying faults in transmission lines with TCSC compensation. The algorithm is based on modal analysis, wavelet transform, and a PNN applied to the reflected and refracted traveling wave patterns. The algorithm uses voltage and current information from both ends of the transmission line and is capable of accurate fault detection, location, and classification. The features of the algorithm include higher speed than previous algorithms, an operation time of less than 3 milliseconds, and the need to measure voltage from only one end of the line for fault discrimination and classification. In reference [19], a new protection method based on fault detection and classification for TCSC-compensated transmission lines is introduced. The method involves calculating the transient

component based on three phases and uses fuzzy decision rules to accurately select the fault phase. This method has been shown by simulations to be effective and reliable for providing unit protection to a TCSC-compensated transmission system. Reference [20] presents a novel method for fault detection in TCSC-compensated transmission lines by using a combination of the second frequency of the current. This method is based on calculating the sum of samples of the second frequency component of the current. The second frequency of the current is calculated, passed through a filter to remove the main frequency, and then through a selective filter to amplify the second frequency. Then, derivatives based on the samples are calculated, and for each sample, the sum of the samples is computed. If the obtained value is greater than a specified threshold, the fault is detected. In reference [21], a fault detection method for power systems equipped with TCSCs connected to wind farms is presented. This method uses frequency feature images extracted from current signals using the SPF technique to train and test an artificial neural network classifier. This fault detection approach is tested and validated on multiple fault and non-fault data on standard systems.

Reference [22] presents a single-ended protection scheme that utilizes the Maximal Overlap Discrete Wavelet Packet Transform (MODWPT) to extract the energy of the post-fault three-phase current signal. This energy feature is then fed into a Bagged Tree Ensemble Classifier for fast and accurate fault type identification. In [23], an advanced hybrid method based on Variational Mode Decomposition (VMD) and the Teager Energy Operator (TEO) is proposed. By analyzing the energy of the dominant frequency component (IMF1) in the three-phase current signal, the algorithm accurately determines the fault location and faulty phase in less than one millisecond, without requiring complex modeling or training data. Simulation results under various conditions confirm that both methods offer high speed, stability, and accuracy even in the presence of noise and non-ideal network conditions.

Reference [24] proposes an efficient time-frequency analysis method that combines entropy with wavelets to identify and classify faults and faulty segments in SSSC-compensated transmission lines. Discrete wavelet transforms and wavelet entropy calculations are used to analyze current and voltage signals during fault conditions. In Reference [25], a new approach based on a correction factor is introduced to enhance

wavelet packet entropy. The wavelet packet entropy characteristics of fault points before and after the SSSC are extracted. Based on these characteristics, a fault location identification method for SSSC-compensated lines is introduced, which can effectively eliminate the expansion and contraction of the distance protection zone caused by the SSSC by coordinating with distance protection. Reference [26] develops a comprehensive protection scheme for SSSC-compensated transmission lines, utilizing the discrete wavelet transform and regression trees. The proposed scheme successfully performs fault detection, classification, and location for the studied transmission lines. In this study, the wavelet transforms reveal hidden information about fault location, which is then used as input to CART. Reference [27] introduces a fault location algorithm for SSSC-compensated transmission lines based on traveling wave theory and wavelet transform. The algorithm applies a modal transform on the signals of currents and voltages sampled at high frequencies. Reference [28] investigates the effect of series and parallel FACTS devices on distance relay operation. A new distance pilot scheme is presented to overcome the issues of underreach/overreach of distance relays in compensated transmission lines. A digital distance relay modeling is also presented to validate the proposed scheme.

In [29], an innovative protection scheme is proposed for double-circuit transmission lines compensated by an SSSC, utilizing a novel index called the Rate of Change of Positive Sequence Active Power Difference (ROCO-PSAPD) for fast and accurate fault detection. The scheme is based on a centralized protection architecture that relies on synchronized PMU measurements from both ends of the line and integrates three complementary algorithms to identify fault type, distinguish between internal and external faults, and mitigate the impact of power oscillations. Without requiring line parameters, injected voltage measurements from the SSSC, or complex settings, the proposed method demonstrates high speed, accuracy, and reliability under challenging conditions such as current/voltage inversion, high-impedance faults, power swings, and load variations. The approach has been validated through more than 1000 diverse simulation scenarios.

Based on a comprehensive review of the related literature, several research gaps have been identified that directly motivate the main idea and technical contributions of this paper. These gaps, observed in the

protection schemes for compensated transmission lines, particularly in the context of SIPC devices, are summarized as follows:

- To date, no dedicated or independent protection method has been proposed for transmission lines compensated by SIPC.
- Most existing methods for other FACTS devices rely on measuring current and voltage from both ends of the line, which requires a data communication system.
- Lightweight statistical indicators such as CUSUM and correlation coefficients have not been employed in previous protection algorithms.
- Many previous methods are based on machine learning techniques, which require large amounts of data for model training and calibration.

**1-4- Contributions and novelties**

This paper proposes a novel, lightweight, yet highly robust algorithm for detecting asymmetrical faults including single-line-to-ground, double-line-to-ground, and line-to-line faults and identifying the faulty section in transmission lines equipped with a SIPC. Unlike many existing techniques that rely on complex machine learning structures or dual-ended measurements, the proposed method requires only three-phase current signals from a single terminal and leverages simple yet effective statistical indicators such as CUSUM and inter-phase correlation coefficients. The core structure of the algorithm comprises two independent but complementary stages. In the first stage, fault occurrence is detected in less than a quarter-cycle by tracking abrupt statistical deviations in the current waveforms using the CUSUM outputs for each phase (denoted as $g_1$ and $g_2$). In the second stage, temporal vectors of the CUSUM outputs are constructed, and the correlation structure between phases is analyzed. A weighted decision-making index based on these correlation coefficients is then compared against threshold values to accurately determine the fault location relative to the SIPC (i.e., before or after the compen and complex training procedures, as well as its real-time capability and high resilience to signal distortion and noise. The unique configuration of SIPC—consisting of two SSSC-based voltage injection units—modifies the dynamic impedance profile of the line and renders many conventional protection strategies ineffective in localizing faults. This work addresses

that critical gap by modeling a detailed SIPC-equipped power system in MATLAB/Simulink and validating the proposed algorithm under realistic and stressed conditions.

To ensure the performance and stability of the proposed method, it was extensively tested across 5,400 different simulation scenarios, including 5,292 fault cases and 108 normal operating conditions. The fault scenarios encompass all possible asymmetrical fault types (single-line-to-ground, three variants of double-line-to-ground, and three types of line-to-line faults), injected at every kilometer of the transmission line and simulated with three different fault resistance values (1, 50, and 100 ohms). The 108 normal scenarios represent transient network conditions without actual faults, including load variation, voltage angle changes, and different SIPC operating modes. This extensive coverage enabled precise determination of optimal threshold values for the algorithm. Specifically, the threshold value for the CUSUM index (g) was set to zero, and 35% was chosen as the threshold for the correlation coefficient (corr). These values were derived from a statistical analysis of the complete dataset, identifying the point of maximum distinction between faulty and non-faulty conditions. Moreover, the sensitivity parameters (v and h) in the CUSUM detection algorithm were also optimized using the same 5,400-case dataset to achieve the best trade-off between detection speed and false alarm reduction.

The results indicate that the algorithm performed correctly in 5,317 out of 5,400 scenarios, with only 83 cases resulting in detection errors most of which occurred under boundary or extreme operating conditions. Based on these outcomes, the overall detection accuracy of the method was calculated to be 98.46%, representing the average performance across all tested cases—not a limited sample. It is widely acknowledged that no protection algorithm can achieve 100% accuracy under all real-world conditions, but the performance observed here demonstrates a high degree of reliability compared to existing standards. Due to space limitations, it was not feasible to present all 5,400 scenarios in the paper. However, the simulation and sensitivity analysis sections include a representative selection of diverse scenarios that cover a wide range of network conditions. These include real fault events as well as critical but non-fault transients such as severe noise, current transformer saturation, high-impedance faults, large load switching, and motor startup events. The sensitivity analysis shows that the proposed algorithm not only accurately detects real

faults but also effectively avoids false alarms in non-fault events. This confirms the algorithm's high degree of stability and discriminative power, and its practical adaptability to the complex behavior of SIPC-compensated lines.

The main contribution of this study lies in the development of a training-free, fast-acting, and compact algorithm that detects faults in less than a quarter-cycle and distinguishes the faulty section with respect to the SIPC location. By combining CUSUM-based statistical analysis with inter-phase correlation modeling, the method delivers a practical and effective framework for fault detection and localization in real-world SIPC-equipped transmission systems.

The contributions of the paper are highlighted and listed below:

1. Proposing a novel algorithm for fault detection and faulty section identification in SIPC-compensated transmission lines.
2. Developing a method tailored to asymmetrical short-circuit fault types, including single-phase-to-ground, two-phase-to-ground, and phase-to-phase faults.
3. Utilizing current signal data measured at a single line terminal to enhance the reliability of the proposed method.
4. Designing a heuristic flowchart and applying cumulative sum and correlation coefficient techniques for effective algorithm implementation.

**1-5- Paper organization**

The paper is organized into seven sections. Section 1 introduces the research background and motivation, and highlights the main challenges associated with fault detection in SIPC-compensated transmission lines. Section 2 presents the basic operational principles and mathematical modeling of the SIPC. Section 3 details the proposed protection algorithm, including the CUSUM-based fault detection strategy, the correlation-based faulty segment identification process, and the complete protection flowchart. Section 4 describes the test network and simulation setup in MATLAB/Simulink. Section 5 provides a comprehensive analysis of twelve diverse asymmetrical fault scenarios to evaluate the algorithm's detection accuracy and localization capability. Section 6 presents a sensitivity analysis of the algorithm under non-ideal operating conditions,

such as noise, CT saturation, heavy load switching, and motor startup. Section 7 compares the proposed method with three recently published techniques and concludes with a performance discussion and summary of findings.

## 2. Static Inter-phase Power Controller

The SIPC equipment is an extension of IPC [3]. The PSTs used in IPC are replaced by SSSCs, which ultimately make SIPC. As shown in Fig. 1(a), each SPC phase contains two SSSC modules. The DC buses of these modules are connected to a common battery, and they are also linked to the AC grid through two coupling transformers to inject phase-shifted voltage. The VSCs are assumed to be lossless, and each is equipped with a pulse width modulation (PWM) controller [3, 30]. A control circuit regulates the amplitude and phase angle of each injected phasor. The VSCs operate as ideal phase angle regulators, allowing active power exchange. Therefore, battery storage equipment must be connected to the DC bus. The VSCs generate sinusoidal voltage at the fundamental frequency. Accordingly, sinusoidal voltage sources denoted by $V_{se1}$ and $V_{se2}$ are used to model these VSCs, as illustrated in Fig. 1(b). Fig. 1(c) presents the phasor diagram of the phase shift angles, which can be used to generate the equivalent circuit. The SIPC's power injection model is introduced in Fig. 2 [3]. The fundamental power equations shown in Fig. 2 indicate that the apparent output power of the SIPC depends on the parameter $\alpha$, while the ratio of active to reactive output power is affected by $\beta$. The locus of the apparent output power of the SIPC is represented as a circle with radius $\rho$max on the Qr–Pr power plane, as shown in Fig. 3. Based on $\rho = -2V_S V_r B_{\text{eq }1} |sin(\alpha)|$, the radius of this circle depends solely on the parameter $\alpha$. Therefore, the apparent power of the SIPC is entirely governed by $\alpha$. For the operating point S0, which includes components $P_0$ and $Q_0$ on a circle of radius ρ, the line connecting this point to the origin forms an angle with the active power axis, as depicted in Fig. 3. This angle is specifically determined by the control variable $\beta$. Hence, the operating point, which includes the active and reactive powers, can be adjusted by changing $\beta$ while keeping the apparent power constant (i.e., $\alpha$ = constant). The apparent power and one of its components (e.g., reactive power) can be set by

simultaneously adjusting $\alpha$ and $\beta$. Fig. 4 shows the block diagrams of the primary controllers based on the described theory [3].

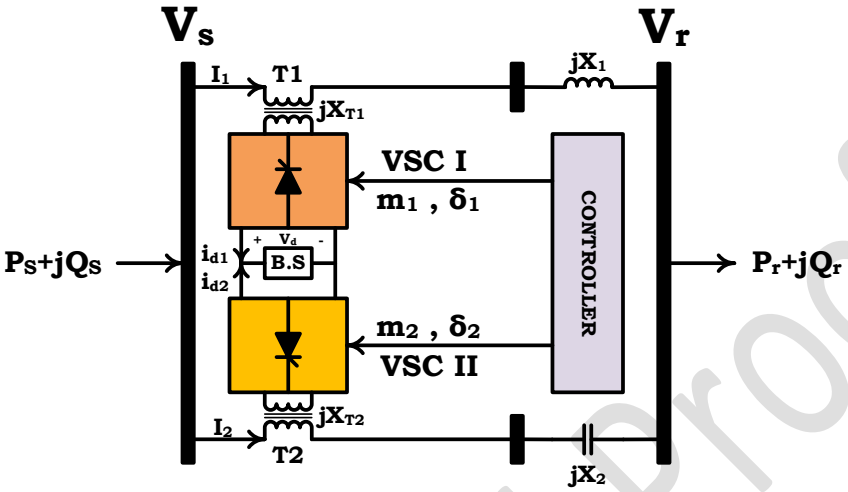


(a)

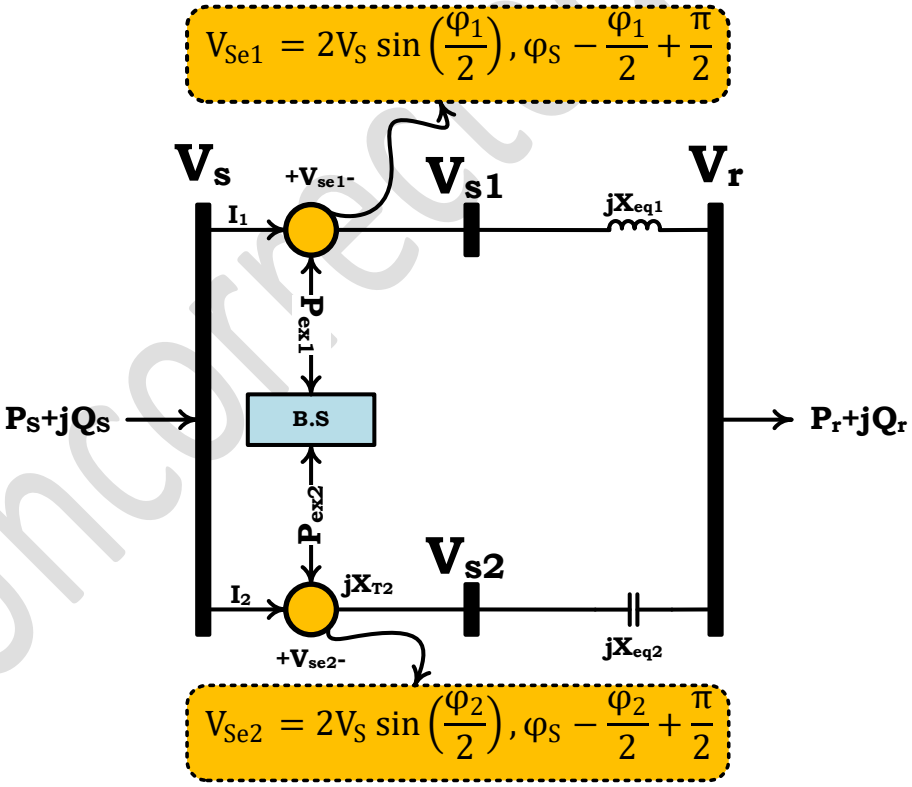


(b)

AUT Journal of Electrical Engineering
10.22060/eej.2025.24075.5651

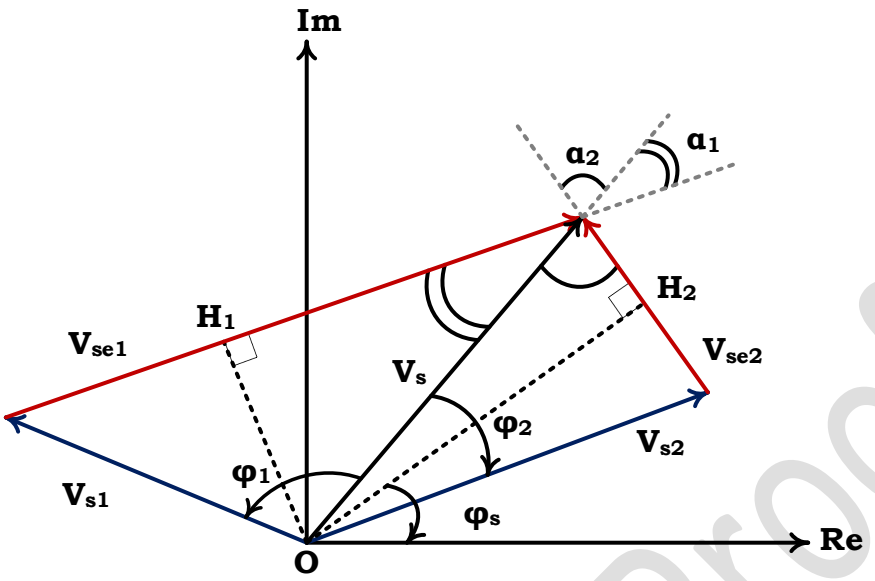


(c)

Fig. 1. SIPC structure (a) single-line diagram, (b) model, and (c) phase-shift angles.

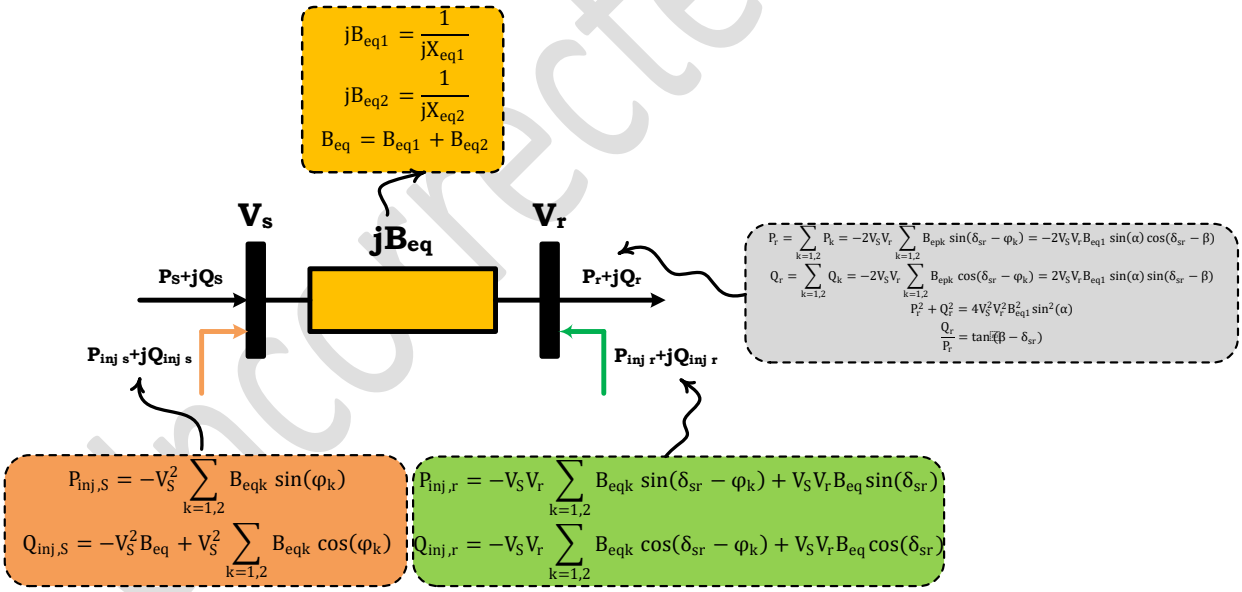


Fig. 2. Power injection model of the SIPC.

10.22060/eej.2025.24075.5651

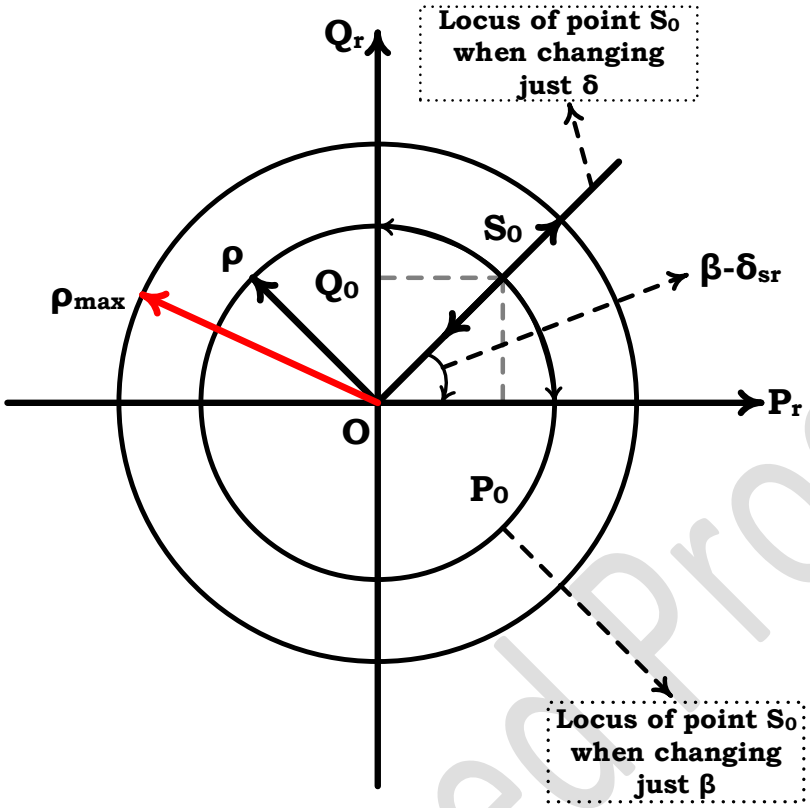


Fig. 3. Locus of output apparent power of the SIPC.

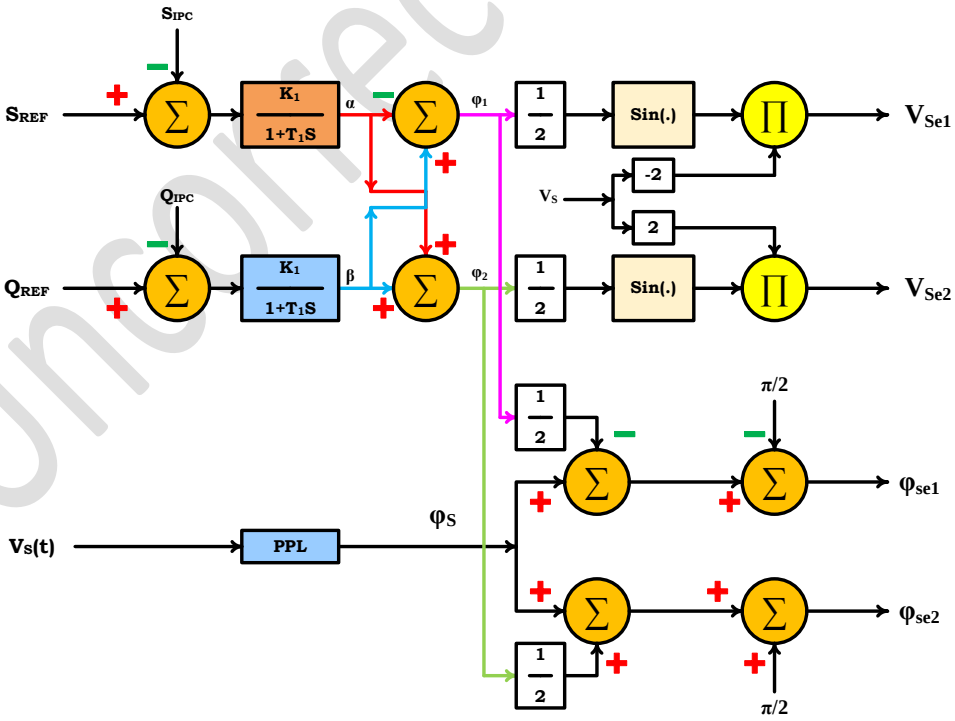


Fig. 4. Control system diagram of the SIPC.

10.22060/eej.2025.24075.5651

## 3. Proposed method

### 3-1-Introducing the general structure of the network under study

Fig. 5 shows the single-line diagram of the network under study. This network consists of a transmission line compensated by an SIPC. The line is modeled on both sides using Thevenin sources. The goal of the algorithm is to determine the fault time and identify the faulty section by measuring the three-phase current at bus S. The algorithm is described in detail below.

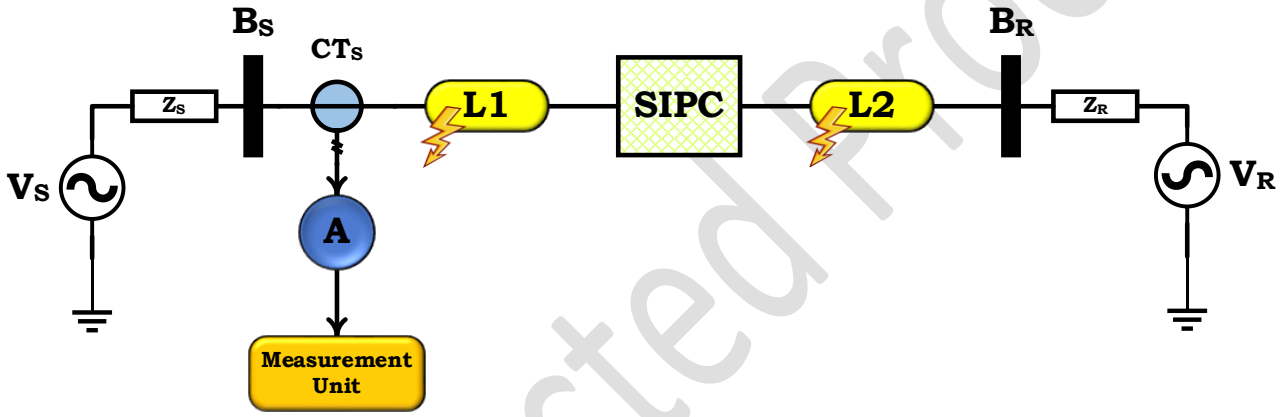


Fig. 5. Single-line diagram of the network under study.

### 3-2- Analysis of the proposed algorithm

#### 3-2-1 Fault detection method

In this section, the cumulative sum algorithm (CSA) is used to detect the occurrence of an asymmetrical short-circuit fault in the network under study, as shown in Fig. 6. CSA is widely applied across various fields to identify sudden changes [31, 32]. A key feature of this algorithm is that a deviation from the initial waveform alone is not sufficient to detect a fault. In CSA, a reference value is defined as the boundary between the network's normal operating state and the fault condition. The algorithm detects a fault only when a deviation from the initial waveform occurs and, during this deviation, the sampled values exceed the reference parameter boundary. To detect faults, the CSA samples the current signal flowing through the

system. At each moment, the sampled value is compared with the maximum allowable limit, and an output index is calculated based on the difference. Since the method is iterative, the index obtained at each stage is passed to the next. By monitoring this output index, fault events in the system can be identified. To apply this algorithm in power system fault detection, a bidirectional CSA must be used due to the sinusoidal nature of the signals [33].

### A. Step 1 of the CSA

To this end, the current signal of the system is sampled, and two parameters are defined as given by Eqs. (1) and (2):

$$S_K(1) = S_K \quad (1)$$

$$S_K(2) = -S_K \quad (2)$$

### B. Step 2 of the CSA

In the second step, the indices of the aggregate sum algorithm are defined using Eqs. (3) and (4):

$$g_K(1) = max\{g_{K-1}(1) + S_K(1) - v, 0\} \quad (3)$$

$$g_K(2) = max\{g_{K-1}(2) + S_K(2) - v, 0\} \quad (4)$$

Selecting the parameter *v* significantly impacts the performance of the algorithm. To use the CSA as a fault detector in the power system, *v* must be set equal to the maximum relay setting current, since the maximum allowable current flowing through the system is always equal to this value. Therefore, whenever a sample value of the current exceeds this limit, it can be evidence of a fault occurrence in the system. To run the algorithm, the initial values of *g* are chosen according to Eq. (5).

$$g_{K-1}(1) = 0, g_{K-1}(2) = 0, k = k_0 \quad (5)$$

10.22060/eej.2025.24075.5651

Now, the CSA can be described as follows. At moment *k*, the *k*th sample is taken. The algorithm calculates the difference between the *k*th sample value and the maximum current amplitude of the relay $S_K(1)$-$v$ , $i$=1,2 and adds this difference to the last index value obtained from the previous step $g_{K-1}(i)$, $i$=1,2.

### C. Step 3 of the CSA

In the third step, the max operator compares the result of the second step with zero. The maximum operator causes the outputs to be zero or a positive value. Considering the initial value of zero for $g_K$ indices, as long as the system works under normal operating conditions, none of the sample values exceed the value *v* and $S_K - v$ is negative. So, the max operator transfers the zero output to $g_K$ indices. Therefore, as long as the system operates under normal conditions, the values of $g_K$ indices are zero. Once a fault appears, the system current rises, so the values of the samples taken exceed the boundary *v*. The necessity of using the bidirectional CSA is seen here. If the fault appears in the positive half-cycle of the current wave, $g(1)$ index starts to grow, and if the fault occurs in the negative half-cycle, $g(2)$ index starts to rise.

### D. Step 4 of the CSA

In the fourth step to boost the reliability of the system, it can be said that if condition (6) is satisfied for three consecutive samples, it is considered a fault:

$$g_K(1) > h \; OR \; g_K(2) > h \qquad (6)$$

where *h* denotes the threshold parameter, which should ideally be chosen equal to zero.

## 3-2-2 Detection method of the faulty section

In this section, the goal is to present an algorithm that can determine the side on which an asymmetrical short-circuit fault occurs in a transmission line with respect to the SIPC. To implement this algorithm, statistical indices of correlation and cumulative sum have been used. In multivariate statistical analyses, the relationship between two random variables and their dependency on each other are measured using various

computational techniques. By the correlation coefficient between any given two variables, we mean predicting the value of one variable in terms of the other variable's value. Calculating correlation coefficients is among the methods used to reveal the relationship between two variables. The larger the value of this index, the greater the relationship or dependence between the two variables. Depending on the type of data, there are different methods for measuring the correlation coefficient. Often, the correlation coefficient shows the relationship between the mean values of two variables. Correlation is used to calculate the similarity between two signals. The correlation relationship is very similar to convolution, with the difference that the second function does not become symmetric. The signal is multiplied by the other signal after being shifted. Whereas in convolution, the signal is multiplied by the shifted symmetry of the second signal. The mathematical definition of correlation is given in Eq. (7).

$$y(t) = x(t)\ o\ h(t) = \int_{-\infty}^{\infty} x(t)h(t-\tau)dt \qquad (7)$$

The advantage of correlation over convolution is that the amount of signal offset, or DC value, is irrelevant to its result. One of the most famous methods of measuring the dependence between two quantitative variables is to find the Pearson correlation coefficient. The Pearson correlation coefficient is calculated as follows. The correlation coefficient between X and Y is represented by $\rho(X,Y)$ or $corr(X<Y)$ and is calculated by Eq. (8).

$$\rho(X,Y) = corr(X,Y) = \frac{E[(X-E(X))(Y-E(Y))]}{[V(X)V(Y)]^{\frac{1}{2}}} \qquad (8)$$

The numerator of this fraction represents the covariance between two variables X and Y. In addition, E is the arithmetic mean of two random variables X and Y.

According to the definition given, the faulty section of the SIPC-compensated transmission line can be determined. First, the relative percentage of correlation between $g_K$ values for the phases of both phases (ab, ac, and bc) should be calculated separately according to Eq. (9). If condition (10) is satisfied for Eq.

(9), the fault is located before the SIPC; otherwise, it is located after the SIPC. According to Eq. (10), *Th*1 is calculated by implementing the scenario of all different cases of asymmetrical short-circuit fault.

$$\frac{[corr(g_{Ka},g_{Kb}),corr(g_{Ka},g_{Kc}),corr(g_{Kb},g_{Kc})]\times 100}{max\{corr(g_{Ka},g_{Kb}),corr(g_{Ka},g_{Kc}),corr(g_{Kb},g_{Kc})\}} = [Corr_{\%}^{ab}, Corr_{\%}^{ac}, Corr_{\%}^{bc}] \quad (9)$$

$$\left[Corr_{\%}^{ab}, Corr_{\%}^{ac}, Corr_{\%}^{bc}\right] > Th1 \quad (10)$$

**3-3- Flowchart of the proposed algorithm**

In this section, the complete flowchart of the protection scheme is presented in Fig. 6. As shown, the flowchart consists of two main parts. The first part involves detecting the occurrence of a fault in the line, and the second part involves identifying the faulty section of the transmission line in question with respect to the SIPC. All the steps described in Subsections 3.1 and 3.2 are included in full and in summary within this flowchart.

10.22060/eej.2025.24075.5651

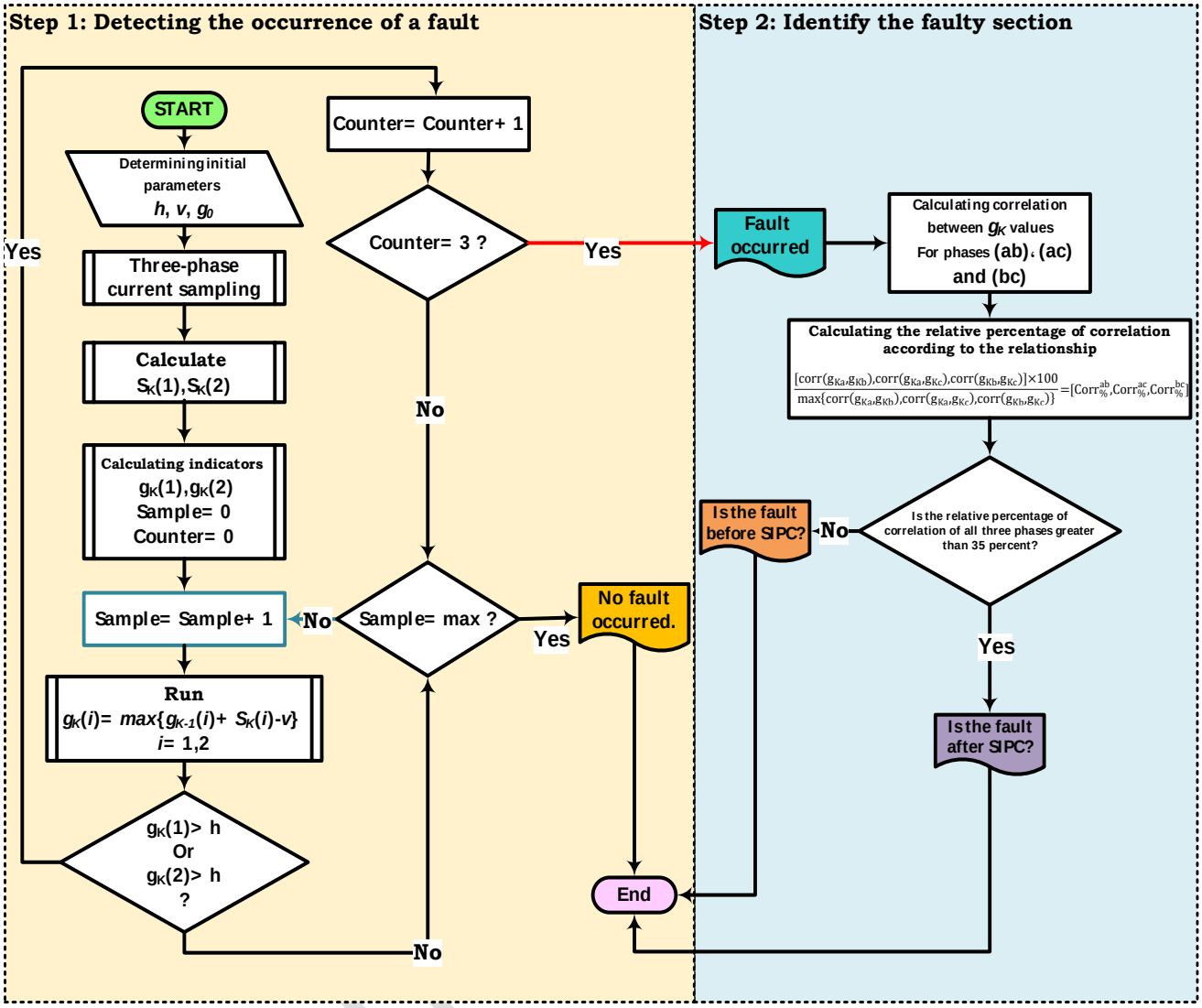


Fig. 6. Complete flowchart of the proposed protection scheme.

## 4. Simulation and results analysis

### 4-1- The tested three-phase network

Fig. 7 illustrates the three-phase diagram of the SIPC-compensated network. The total length of the line is 200 km, and the SIPC is installed at the midpoint. The network under study operates at a voltage of 230 kV and a frequency of 60 Hz. Information about the line parameters, the Thevenin sources on both sides of the line, and the SIPC settings is provided in Table 1. The studied network is simulated using the Simulink platform of MATLAB software, and the proposed algorithm is programmed in an m-file.

AUT Journal of Electrical Engineering
10.22060/eej.2025.24075.5651

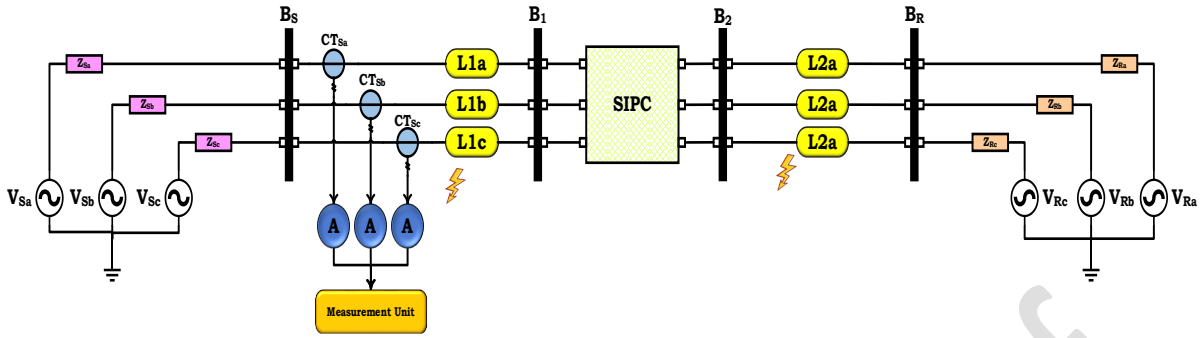


Fig. 7. The test networks.

Table 1. Network specifications.

| Specifications of the lines | | | | | |
|---|---|---|---|---|---|
| **Parameter** | **Value** | **Parameter** | **Value** | **Parameter** | **Value** |
| $r_1$(Ohms/km) | 0.0529 | $l_1$(H/km) | 0.0014 | $c_1$(F/km) | $8.7751\times10^{-9}$ |
| $r_0$(Ohms/km) | 0.3864 | $l_0$(H/km) | $4.1264\times10^{-3}$ | $c_0$(F/km) | $7.751\times10^{-9}$ |
| F (Hz) | 60 | Phase | 3 | V (V) | $230\times10^{3}$ |
| **Specifications of the power sources** | | | | | |
| Parameter | Value | Parameter | Value | Parameter | Value |
| Phase-to-phase voltage ($V_{rms}$) (kV) | 230 | The phase angle of Bus S | 20 | Frequency (Hz) | 60 |
| 3-phase short-circuit level at base voltage (VA) | $900\times10^{6}$ | The phase angle of Bus R | 0 | X/R ratio | 7 |
| **Specifications of the SIPC** | | | | | |
| Series controller 2 | | Series controller 1 | | Specifications of the converters | |
| **Parameter** | **Value** | **Parameter** | **Value** | **Parameter** | **Value** |
| K1 | 1 | K1 | 1 | Power Electronic device | GTO |
| T1 | 10 | T1 | 10 | Snubber resistance Rs (Ω) | $1\times10^{5}$ |
| L (H) | 0.0068 | C (F) | 0.001 | Internal resistance Ron (Ω) | $1\times10^{-4}$ |



### 4-1- Analysis of different fault scenarios in the test network

In this section, the aim is to examine in detail the 12 asymmetric short-circuit fault scenarios in the network shown in Fig. 7. These scenarios involve different faults in various phases, at different distances, and with

10.22060/eej.2025.24075.5651

varying resistances on both sides of the SIPC. The results of implementing these scenarios are presented below.

**4-2-1 Scenario 1**

In this scenario, it is assumed that at time $t$ = 0.05 seconds, an ag fault with a resistance of 1 ohm occurred at a distance of 25 km from terminal S. The three-phase current diagram of terminal S ($S_1$ = a (A), $S_2$ = b (B), $S_3$ = c (C)) is shown in Fig. 8. The results of implementing the $g$ index have been calculated for all three phases. In the section related to the CSA indices, it can be seen that, considering the fault in the positive half-cycle, the $g_I$ index initially increases. Due to the presence of a large DC component in the signal, the increasing trend of $g_I$ continues. The strong stability of the CSA indices is clearly evident in this figure. According to the obtained results, as shown, $g_{Ia}$ has increased from zero in the first quarter-cycle of the fault, which indicates fault detection in the transmission line. After correctly identifying the fault occurrence time, the next step is to locate the faulty section with respect to the SIPC. In Fig. 9, the correlation index between the $g_I$ values is shown, which is used as a criterion to identify the faulty segment. Finally, using the results obtained from the pairwise correlation index $g_I$ of both phases, the relative percentage of correlation between the two phases can be calculated. Fig. 10 shows the results of this evaluation. As shown, the value of this relative percentage for phases *a* and *b* exceeds 0.35, which indicates the faulty section. Based on the obtained result, the fault occurred in the section between bus S and the SIPC.

10.22060/eej.2025.24075.5651

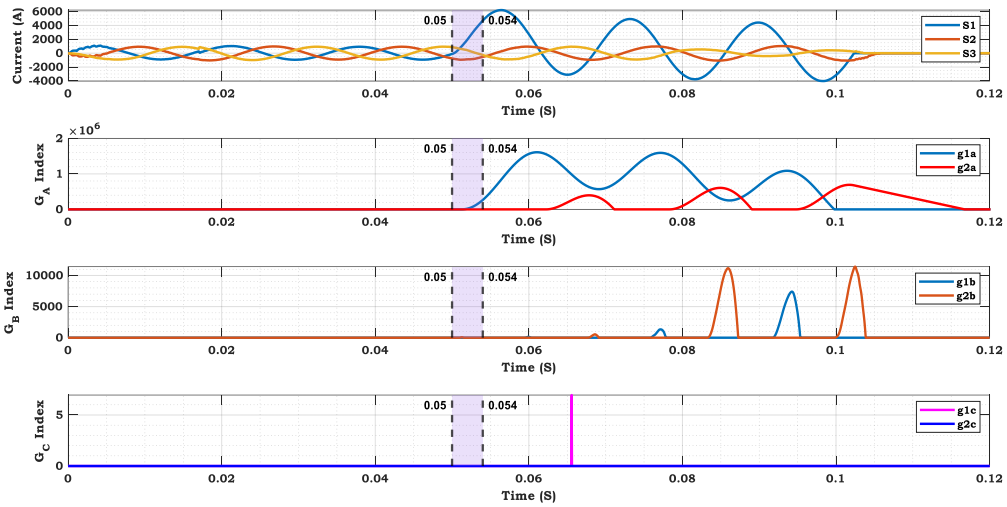


Fig. 8. Three-phase current waveforms and *g* indices in Scenario 1.

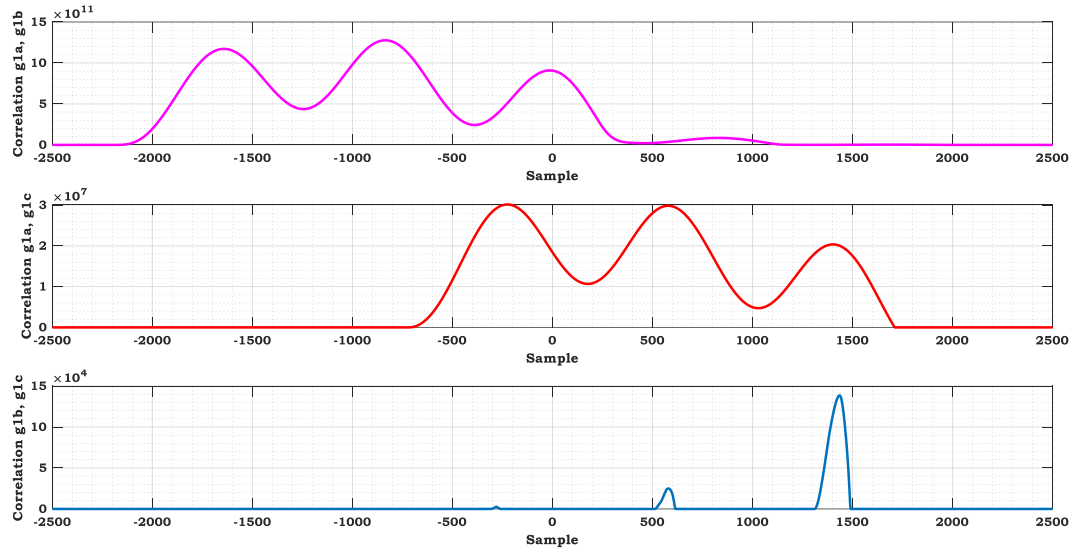


Fig. 9. Correlation index for *g* coefficients in scenario 1.

10.22060/eej.2025.24075.5651

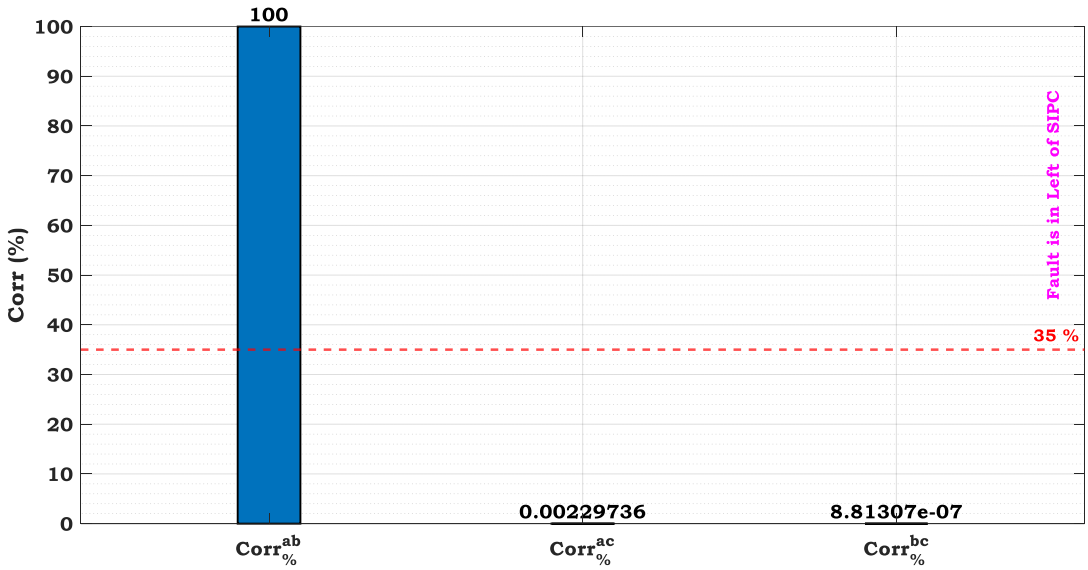


Fig. 10. Faulty segment detection index in Scenario 1.

### 4-2-2 Scenario 2

Scenario 2 assumes that a phase-to-phase fault between phases *a* and *b*, with a fault resistance of 100 ohms, occurred at a distance of 25 km from bus S at time $t$ = 0.05 seconds. According to Fig. 11, the results of measuring the three-phase current and the *g* index of the phases are presented. As shown, the *g* index for phases *a* and *b* increased from zero during the time interval from 0.05 to 0.054 seconds. This indicates the occurrence of a fault in the transmission line. According to the results, the strong stability of the CSA indices in this figure is quite evident. Next, in Fig. 12, the correlation index for the *g* coefficients of both phases in Scenario 2 is shown. Based on the results in Fig. 12, the value of the correlation index between the $g_I$ values is illustrated in Fig. 13, which is used as a criterion to detect the faulty section. As shown, the value of this index for phases *a* and *b* exceeds the threshold of 0.35, indicating a fault in the section between bus S and the SIPC.

10.22060/eej.2025.24075.5651

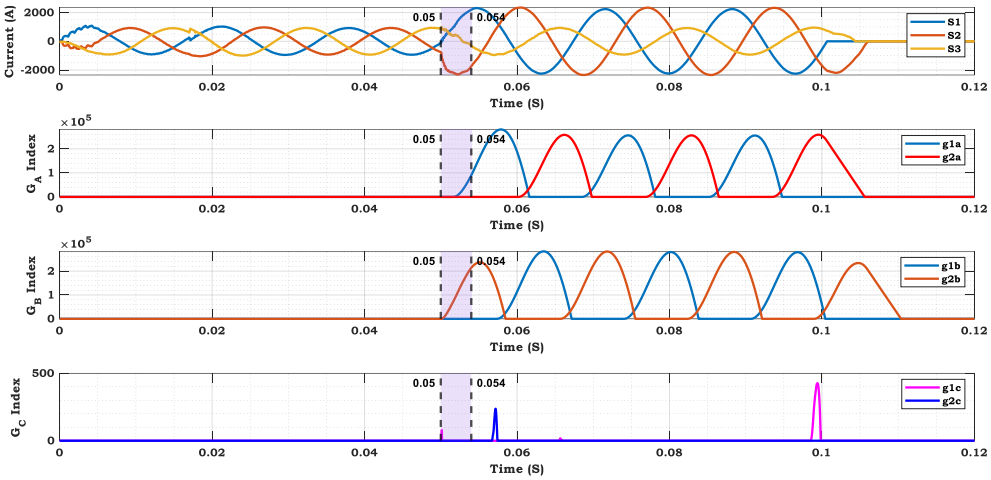


Fig. 11. Three-phase current waveforms and *g* indices in Scenario 2.

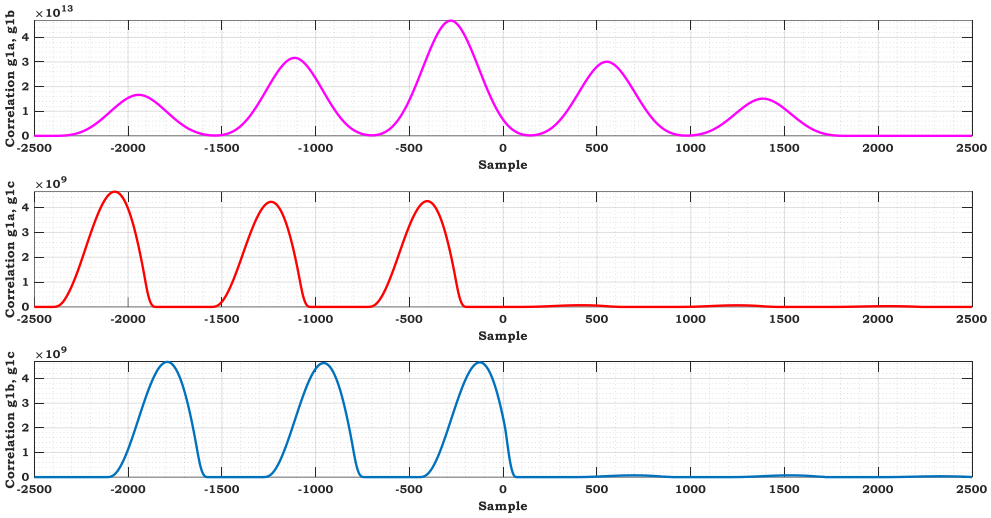


Fig. 12. Correlation index for *g* coefficients in Scenario 2.

10.22060/eej.2025.24075.5651

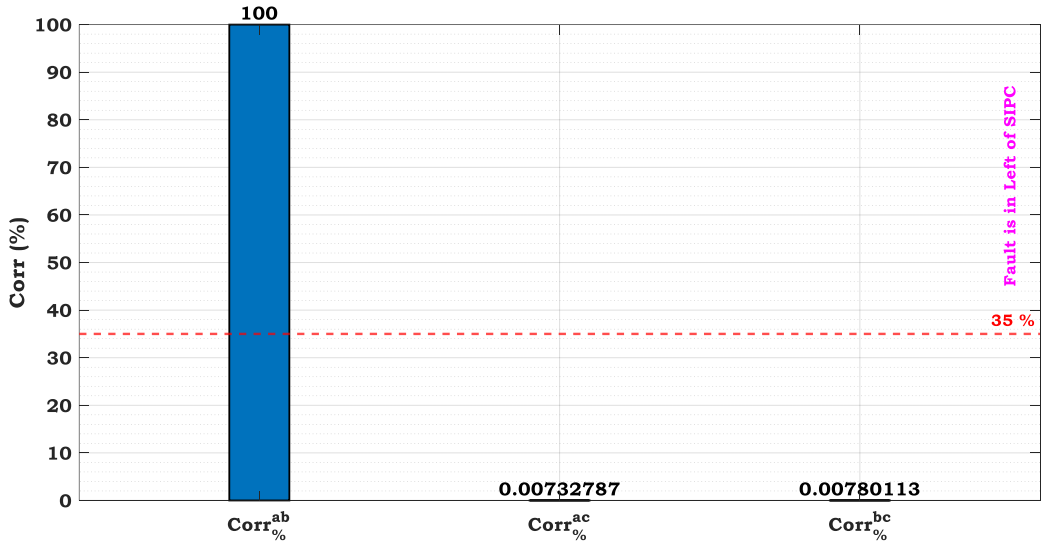


Fig. 13. Faulty segment detection index in Scenario 2.

### 4-2-3 Scenario 3

Scenario 3 assumes that a *bc* fault occurred at a distance of 50 km from bus S, with a resistance of 1 ohm, at time $t$ = 0.05 seconds. Fig. 14 shows the three-phase flow diagram and the $g$ index of all three phases for $g_1$ and $g_2$. As shown, $g_1$ for phase $c$ and $g_2$ for phase $b$ have increased from the zero-threshold value, indicating the occurrence of a fault within a quarter of the fault detection cycle. In the section related to the algorithm indices, a cumulative sum is observed. Considering that the fault in phase $b$ occurs in the negative half-cycle, the $g_2$ index grows first. Due to the presence of a large DC component in the signal, the upward trend of $g_2$ continues. As the wave enters the positive half-cycle, $g_1$ also grows and then returns to zero. The same behavior is observed for phase $c$, and the algorithm successfully detects the fault. Due to the increase in the value of $g$ within the quarter cycle of the fault detection period, it is evident that the fault occurred during this interval and was correctly identified by the algorithm. Subsequently, Fig. 15 plots the correlation index for the $g$ coefficients in Scenario 3 for the two phases. Based on the results obtained in this section, the faulty section detection index in Fig. 16 is calculated for Scenario 3. According to the findings, for both phases $b$ and $c$, the index value exceeds the threshold of 0.35, indicating fault occurrence between bus S and the SIPC installation bus.

10.22060/eej.2025.24075.5651

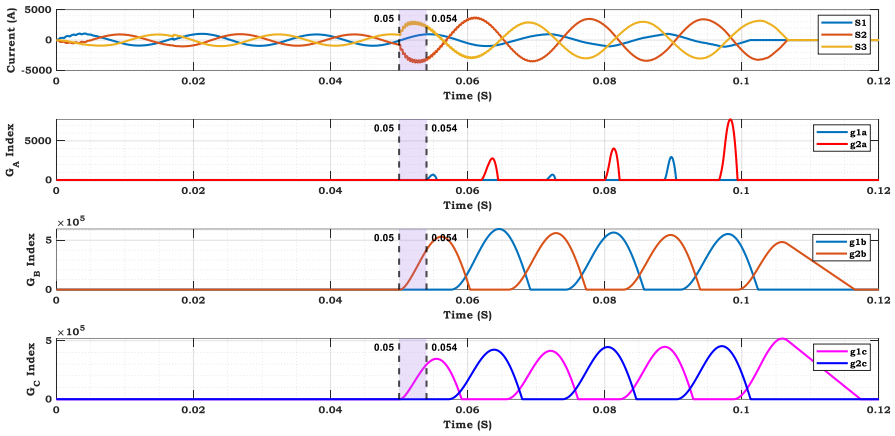


Fig. 14. Three-phase current waveforms and *g* indices in Scenario 3.

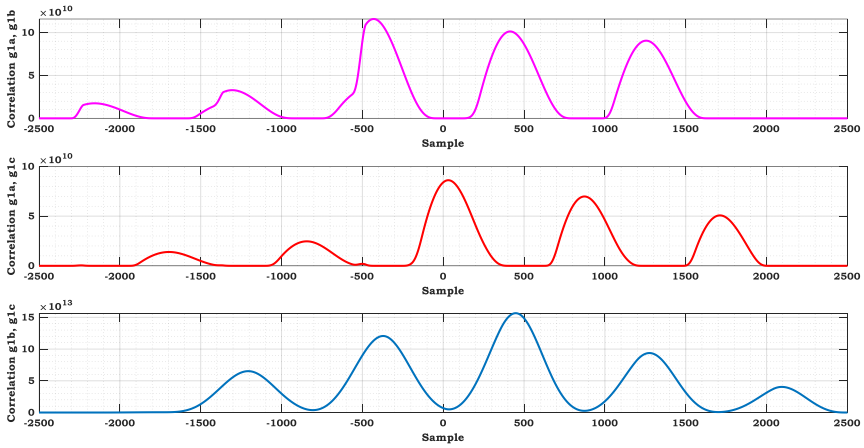


Fig. 15. Correlation index for *g* coefficients in Scenario 3.

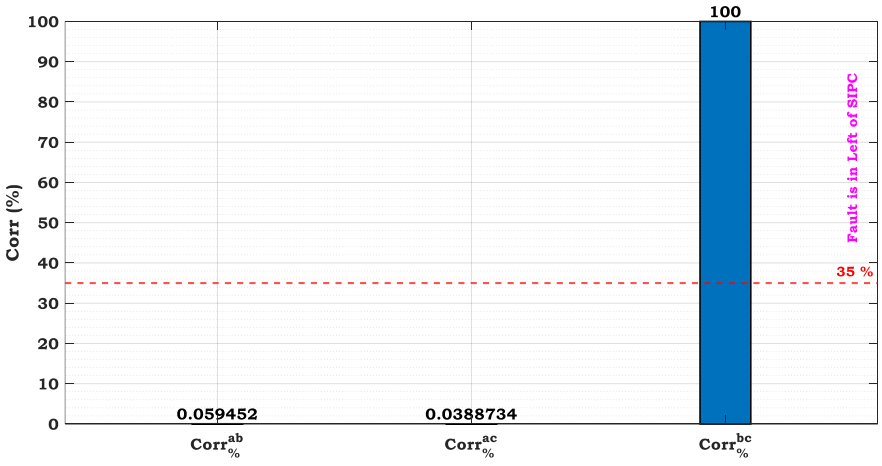


Fig. 16. Faulty segment detection index in Scenario 3.

10.22060/eej.2025.24075.5651

**4-2-4 Scenario 4**

In Scenario 3, it is assumed that a *bg* fault occurs at a distance of 50 km from bus S, with a resistance of 100 ohms, at time $t$ = 0.05 seconds. In Fig. 17, the results of the three-phase current measured from bus S, along with the $g$ values for all three phases for $g_1$ and $g_2$, are plotted. Given that the fault appears in phase *b* during the negative half-cycle, the $g_2$ index increases first. Due to the presence of a large DC component in the signal, the upward trend of $g_2$ continues. This is because the change in the $g$ value for phases *a* and *c* during the detection interval—from $t$ = 0.05 to $t$ = 0.054 seconds—is nearly zero, while for phase *b*, the $g$ value increases from zero within this interval. This indicates correct fault detection by the algorithm within the available detection time. Additionally, Fig. 18 shows the results of implementing pairwise phase correlation. Based on the results plotted in this figure, it is observed that the fault section detection index in Fig. 19 for Scenario 4—corresponding to both phase pairs *a*–*b* and *b*–*c*—exceeds the threshold value of 0.35, indicating the occurrence of a fault in the section between bus S and the SIPC bus.

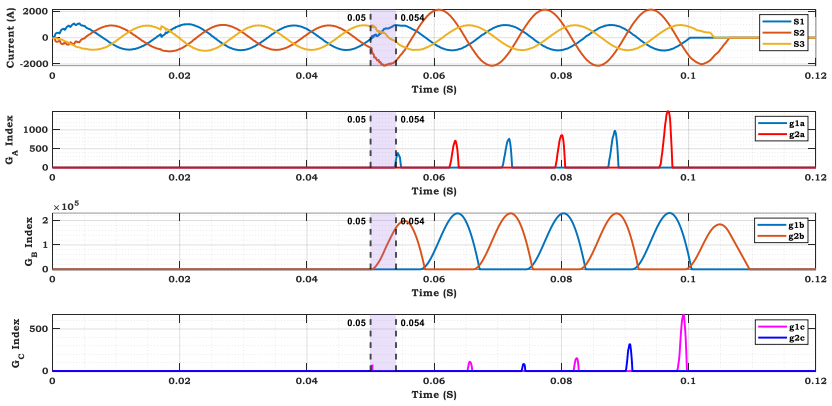


Fig. 17. Three-phase current waveforms and $g$ indices in Scenario 4.

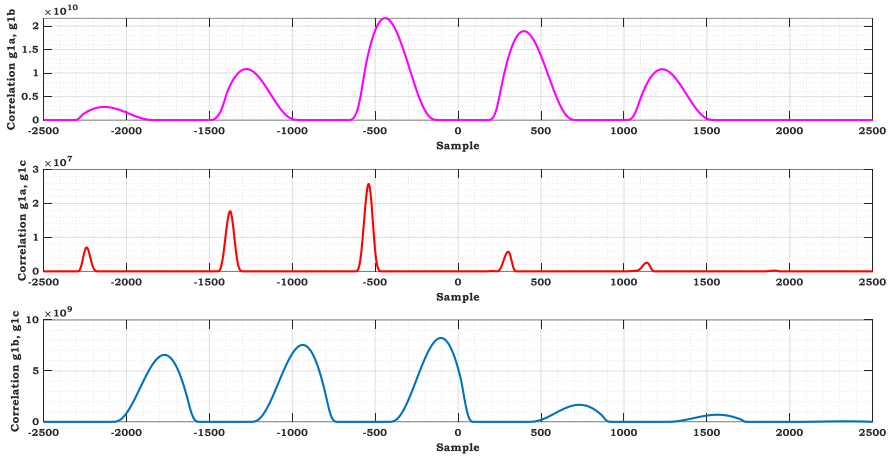


Fig. 18. Correlation index for *g* coefficients in Scenario 4.

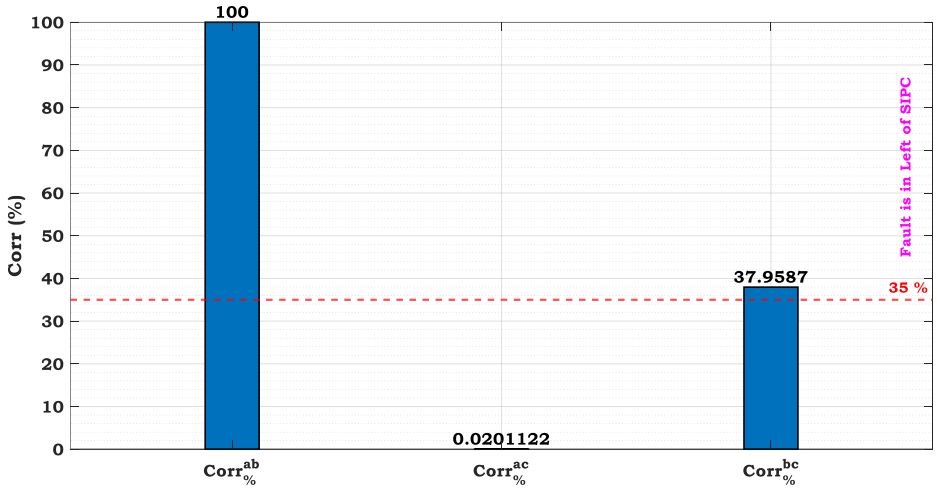


Fig. 19. Faulty segment detection index in Scenario 4.

### 4-2-5 Scenario 5

Scenario 5 assumes a phase-to-phase fault between phases *a* and *c* at a distance of 75 km, with a fault resistance of 1 ohm, occurring at time $t = 0.05$ seconds. In the section related to the CSA indices shown in Fig. 20, it can be seen that, since the fault in phase *a* occurs during the positive half-cycle, the $g_2$ index increases first. Due to the presence of a large DC component in the signal, the upward trend of $g_2$ continues. This also applies to phase *c*, while the *g* value for phase *b* remains zero during the interval from $t = 0.05$ to $t = 0.054$ seconds. Next, in Fig. 21, the correlation index results for the *g* coefficients of both phases are plotted together. These results are used to calculate the fault section detection index. According to the

findings, as shown in Fig. 22, the index value for phases *a* and *c* exceeds the threshold, indicating that a fault has occurred in the section between the SIPC and bus S.

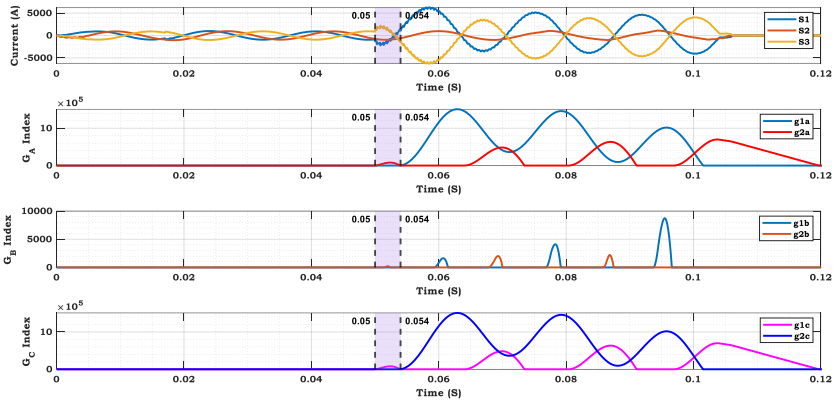


Fig. 20. Three-phase current waveforms and *g* indices in Scenario 5.

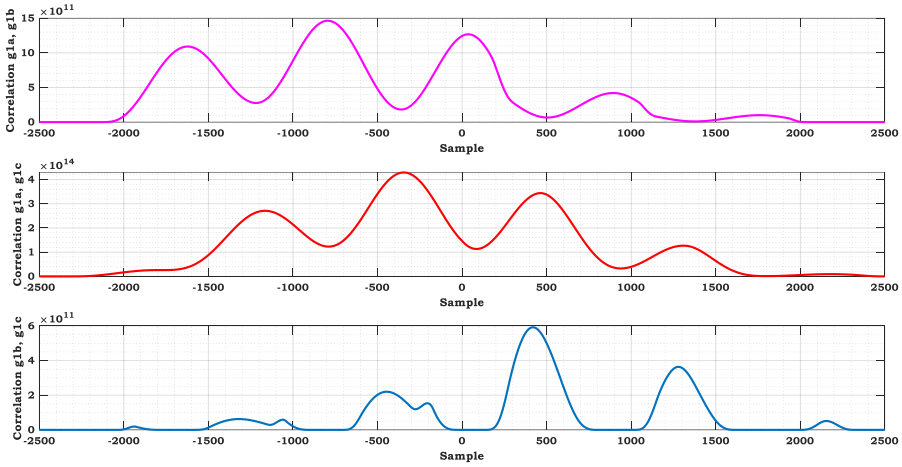


Fig. 21. Correlation index for *g* coefficients in Scenario 5.

10.22060/eej.2025.24075.5651

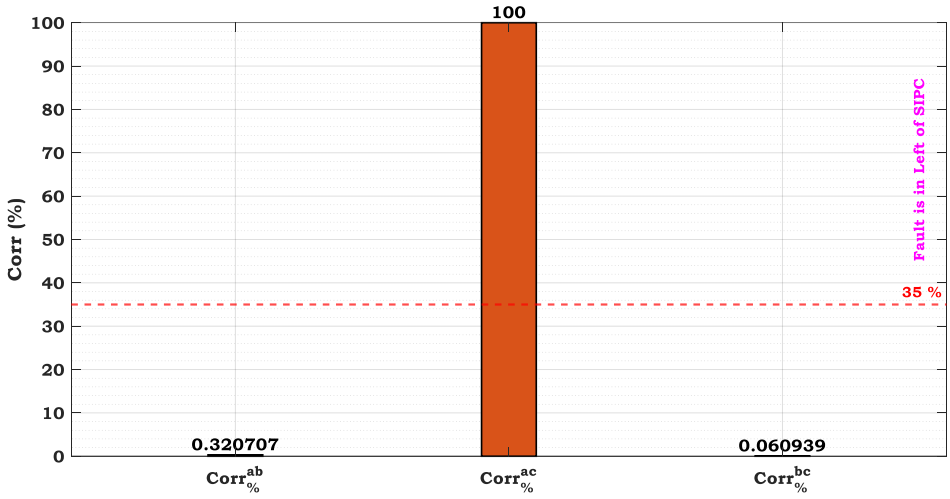


Fig. 22. Faulty segment detection index in Scenario 5.

### 4-2-6 Scenario 6

Scenario 6 assumes that a *cg* fault occurred at a distance of 85 km, with a resistance of 100 ohms, at time $t$ = 0.05 seconds. In Fig. 23, the current of the three phases at terminal S is shown. Based on the measured current, the $g$ values for all three phases are plotted. According to the results, for phases *b* and *c*, the measured $g$ values exceed the zero threshold during the interval from $t$ = 0.05 to $t$ = 0.054 seconds, indicating fault detection within this time interval. In Fig. 24, the results of measuring and calculating the correlation between the two phases based on the $g$ index are plotted. According to the results shown in Fig. 25, which are based on the correlation index, the fault detection index for phases *b* and *c* is greater than the threshold value of 0.35, indicating the occurrence of a fault in the section between bus S and the SIPC installation bus.

10.22060/eej.2025.24075.5651

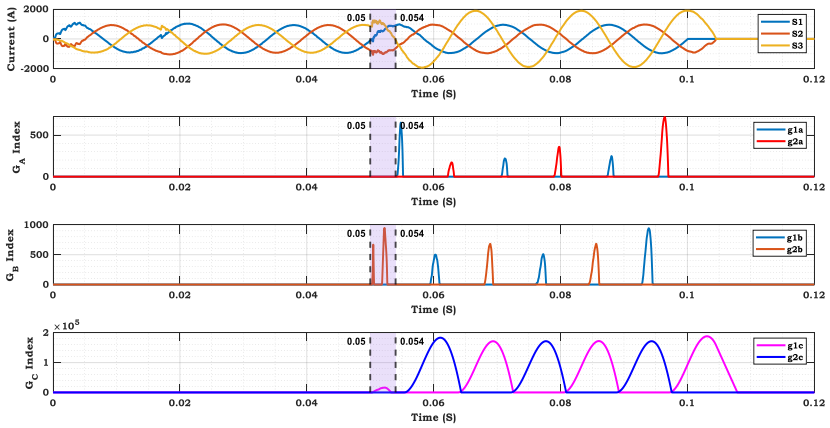


Fig. 23. Three-phase current waveforms and *g* indices in Scenario 6.

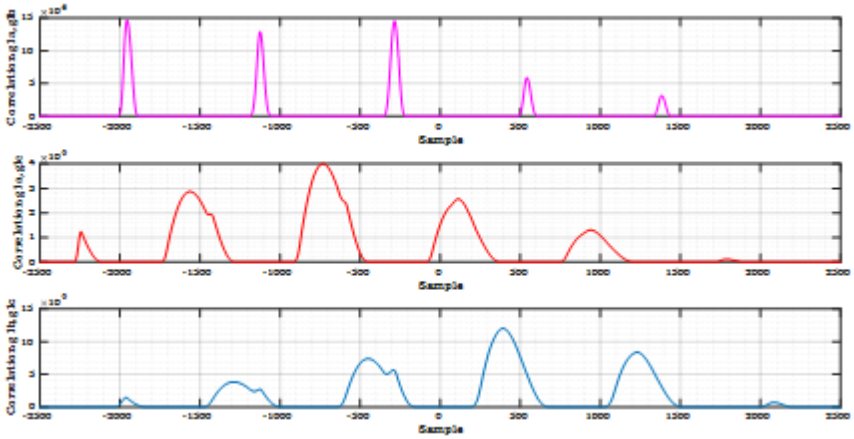


Fig. 24. Correlation index for *g* coefficients in Scenario 6.

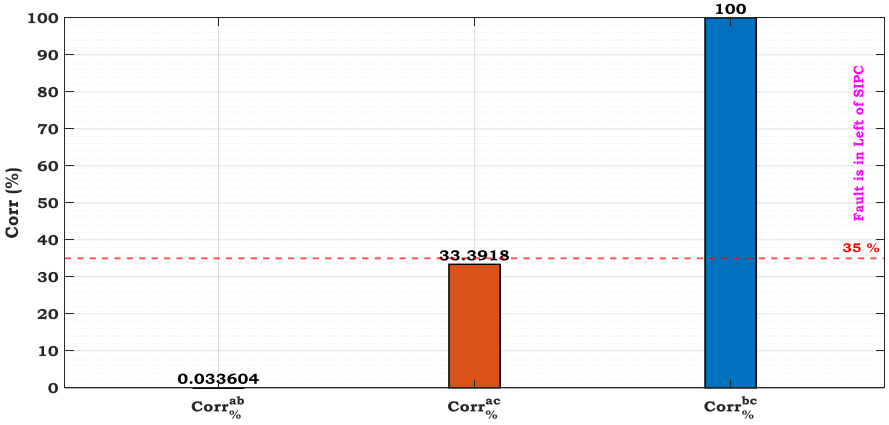


Fig. 25. Faulty segment detection index in Scenario 6.

10.22060/eej.2025.24075.5651

**4-2-7 Scenario 7**

Scenario 7 assumes that an *ag* fault occurred at a distance of 125 km from bus S at time $t$ = 0.05 seconds. The fault resistance is considered to be 1 ohm. In Fig. 26, the three-phase current measured from bus S is shown. According to the results presented in this figure, two $g$ indices have been measured and calculated for all three phases. Considering that the fault detection time for the proposed algorithm is a quarter of a cycle, the results in Fig. 27 show that during the interval from $t$ = 0.05 to $t$ = 0.054 seconds, the $g$ amplitude for all three phases increases from nearly zero. This increase in $g_2$ is most prominent in phase $b$, indicating the occurrence of a fault in the target line. Subsequently, the correlation index signal for the $g$ coefficients in Scenario 7 is shown in a pairwise format for both phases. Based on the results, the fault detection index in Fig. 28 has been calculated. According to these results, all three measured indicators in this figure exceed the threshold value, confirming fault occurrence in the section between bus R and the SIPC installation bus.

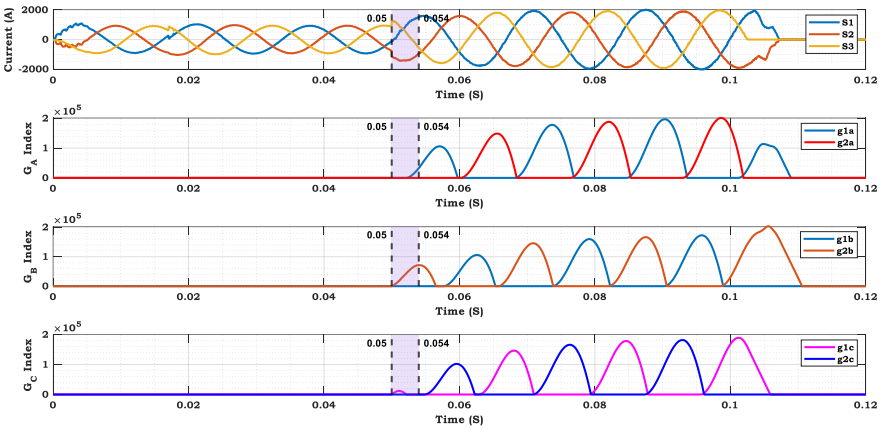


Fig. 26. Three-phase current waveforms and $g$ indices in Scenario 7.

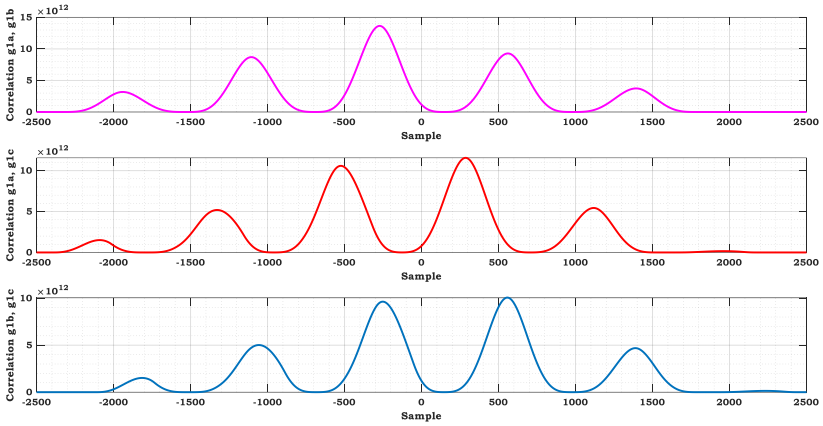


Fig. 27. Correlation index for *g* coefficients in Scenario 7.

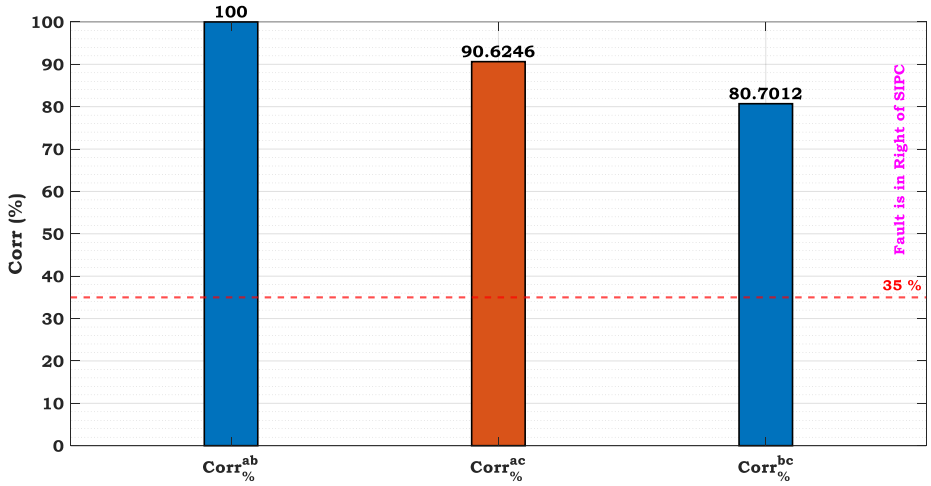


Fig. 28. Faulty segment detection index in Scenario 7.

### 4-2-8 Scenario 8

Scenario 8 assumes that an *ag* fault occurred at a distance of 125 km from bus S, with a resistance value of 100 ohms. The three-phase current signals measured from bus S for this fault are shown in Fig. 29. In the same figure, the *g* values for all three phases are presented based on $g_1$ and $g_2$. According to the results obtained, each *g* index for all three phases exceeds the zero threshold during the time interval from $t = 0.05$ to $t = 0.054$ seconds, indicating the occurrence of a fault. The proposed algorithm successfully detects the fault during this period. In the next section, Fig. 30 shows the results of implementing the correlation coefficients between the phases, and based on these, Fig. 31 presents the values of the fault detection index.

10.22060/eej.2025.24075.5651

According to the results in Fig. 31, the measured indices for both phase pairs exceed the threshold value, confirming that the fault occurred in the section between bus R and the SIPC installation bus.

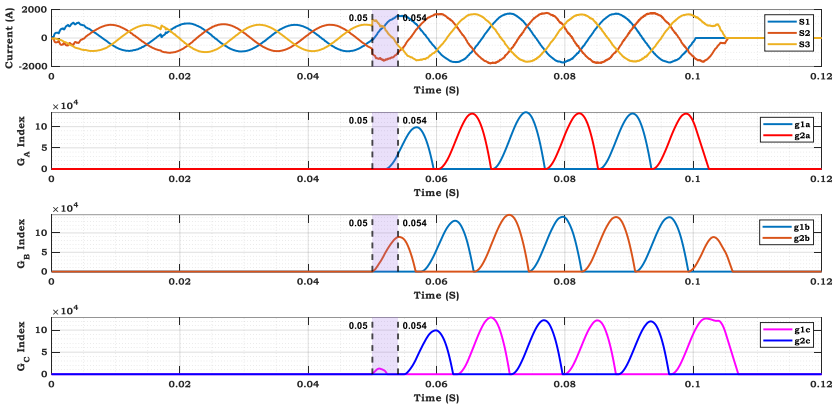


Fig. 29. Three-phase current waveforms and *g* indices in Scenario 8.

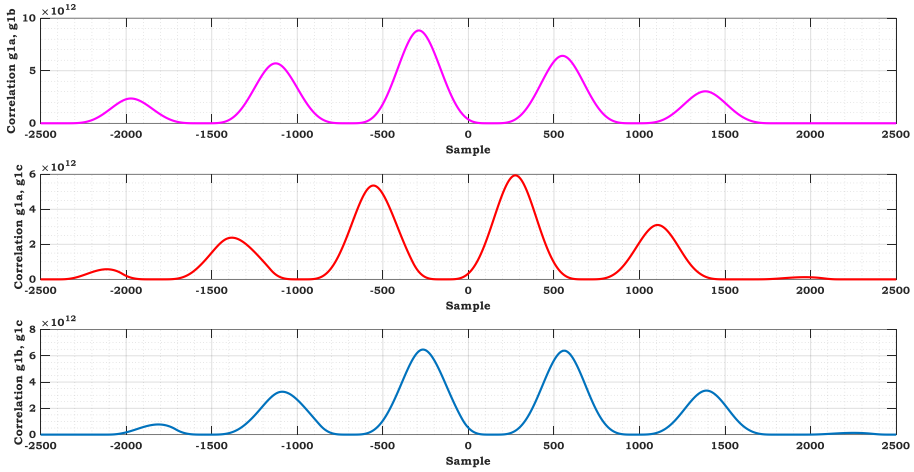


Fig. 30. Correlation index for *g* coefficients in Scenario 8.

10.22060/eej.2025.24075.5651

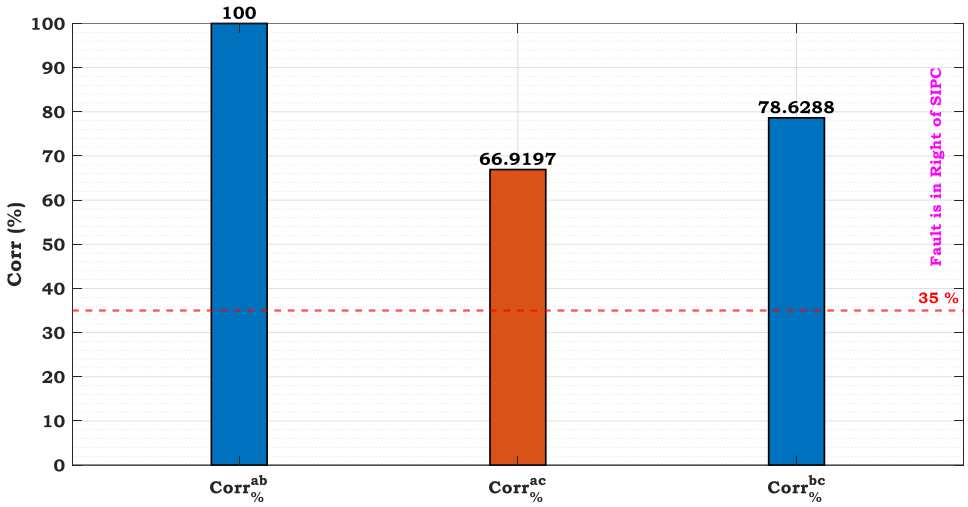


Fig. 31. Faulty segment detection index in Scenario 8.

### 4-2-9 Scenario 9

Scenario 9 assumes a phase-to-phase fault between phases b and c has occurred at a distance of 150 km from bus S. This fault occurred at time t = 0.05 seconds and was considered for fault detection until t = 0.054 seconds. The results of the three-phase measurements from terminal S are shown in Fig. 32. According to these results, for the two g indices across all three phases, the values of $g_1$ have exceeded the threshold of zero, indicating the occurrence of a fault on the specified line. Subsequently, the correlation results between the two phases are calculated and plotted in Fig. 33, according to which, the fault detection index is derived as shown in Fig. 34. Given that all three values exceed the threshold of 0.35, it is concluded that the fault appears in the right section of the SIPC—specifically, in the section between bus R and the SIPC.

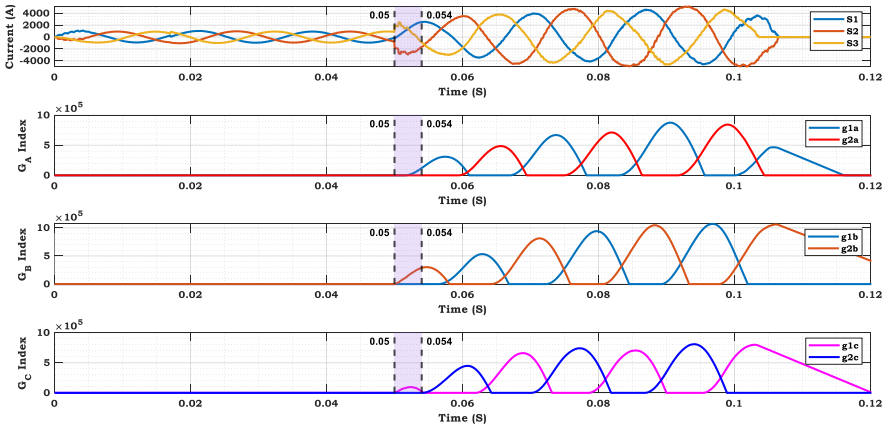


Fig. 32. Three-phase current waveforms and *g* indices in Scenario 9.

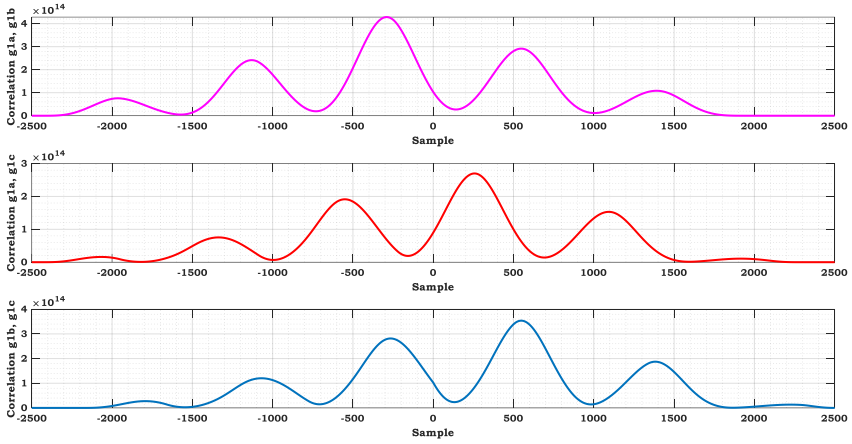


Fig. 33. Correlation index for *g* coefficients in Scenario 9.

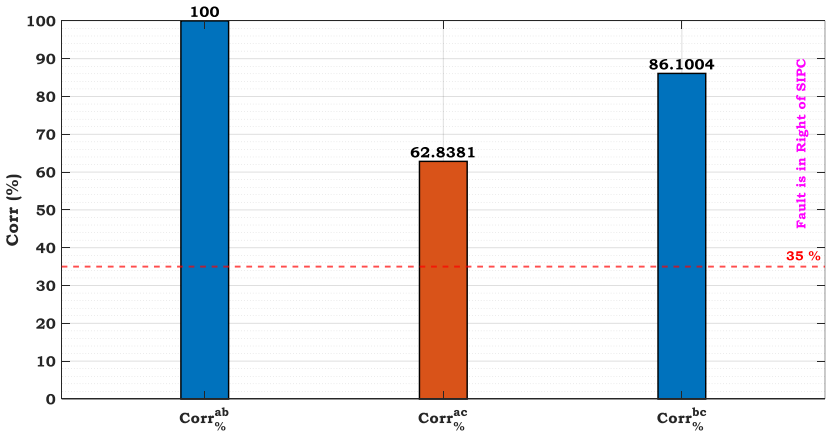


Fig. 34. Faulty segment detection index in Scenario 9.

10.22060/eej.2025.24075.5651

**4-2-10 Scenario 10**

Scenario 10 assumes a bg fault has occurred at a distance of 150 km at time t = 0.05 seconds. The fault resistance in this scenario is considered to be 100 ohms. The results of the three-phase current measurements, as well as the g index for all three phases, are presented in Fig. 35. According to the results, the values of $g_1$ for phase a, $g_2$ for phase b, and $g_1$ for phase c have exceeded the threshold, indicating that a fault has occurred in the system. Additionally, the values of the correlation coefficient and the faulty section detection index are shown in Figs. 36 and 37. Based on the results, it is evident that all three measured values in Fig. 37 are greater than the threshold. This confirms that the fault happens on the right side of the SIPC, i.e., on the line between bus R and the SIPC.

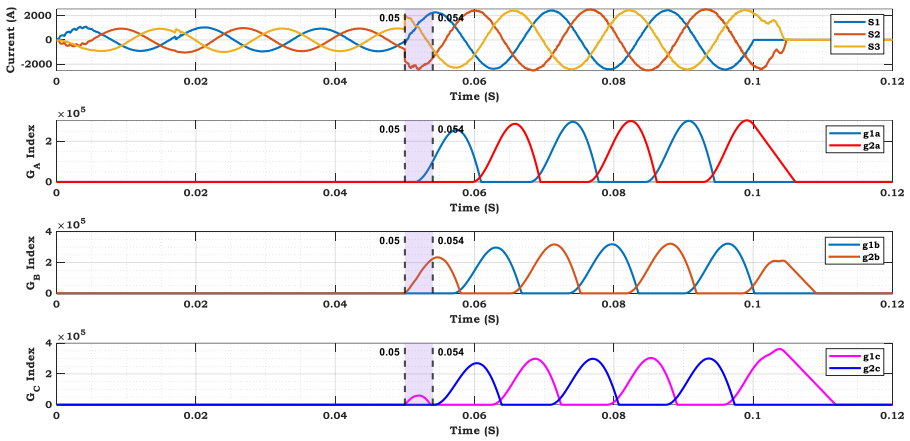


Fig. 35. Three-phase current waveforms and *g* indices in Scenario 10.

10.22060/eej.2025.24075.5651

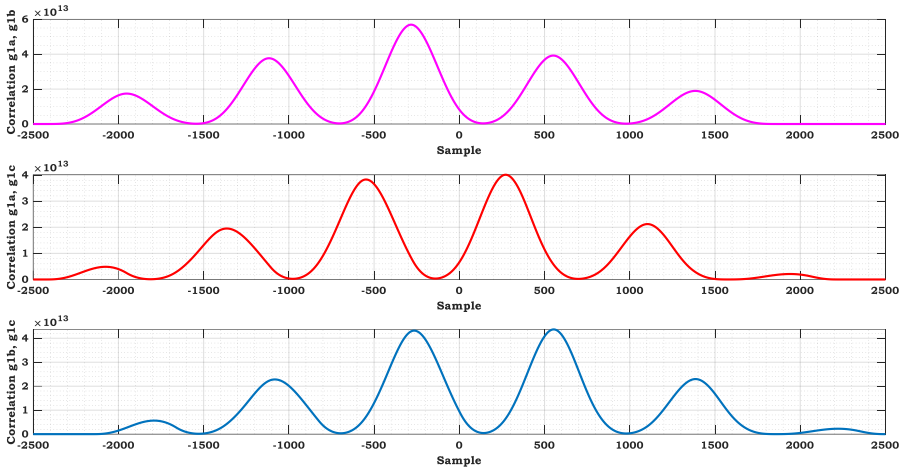


Fig. 36. Correlation index for *g* coefficients in Scenario 10.

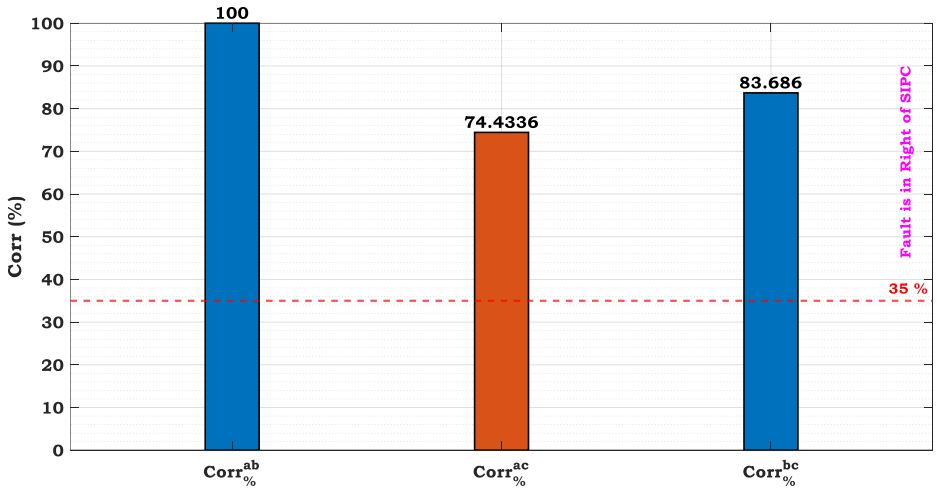


Fig. 37. Faulty segment detection index in Scenario 10.

### 4-2-11 Scenario 11

Scenario 11 assumes an ag fault has occurred at a distance of 175 km from bus S, with a fault resistance of 1 ohm. The three-phase current values measured at bus S are shown in Fig. 38. This figure also includes the calculated g index results for all three phases. According to the figure, the g values for all three phases rise above zero during the time interval from t = 0.05 to t = 0.054 seconds. Based on these results, it is evident that a fault has occurred in the network. Next, Fig. 39 presents the pairwise correlation diagram of the phases based on the g index, and from this, the fault section detection index values for both phases are

calculated and shown in Fig. 40. Since these values for the two phases exceed the threshold of 0.35, it is concluded that the fault has occurred on the line between bus R and the SIPC installation bus.

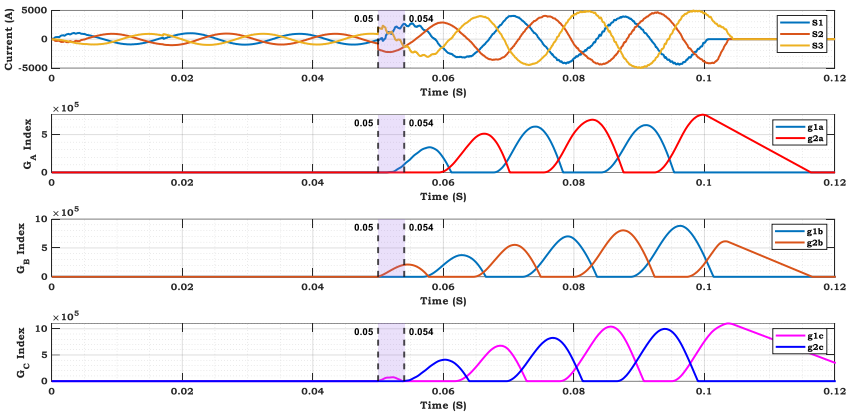


Fig. 38. Three-phase current waveforms and *g* indices in Scenario 11.

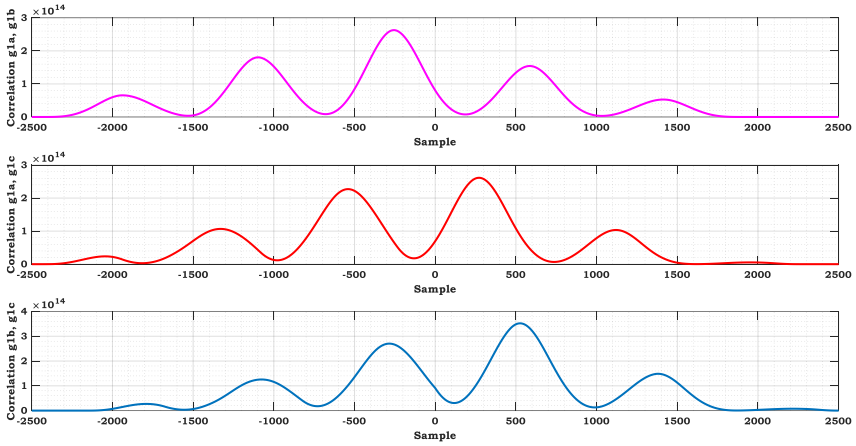


Fig. 39. Correlation index for *g* coefficients in Scenario 11.

10.22060/eej.2025.24075.5651

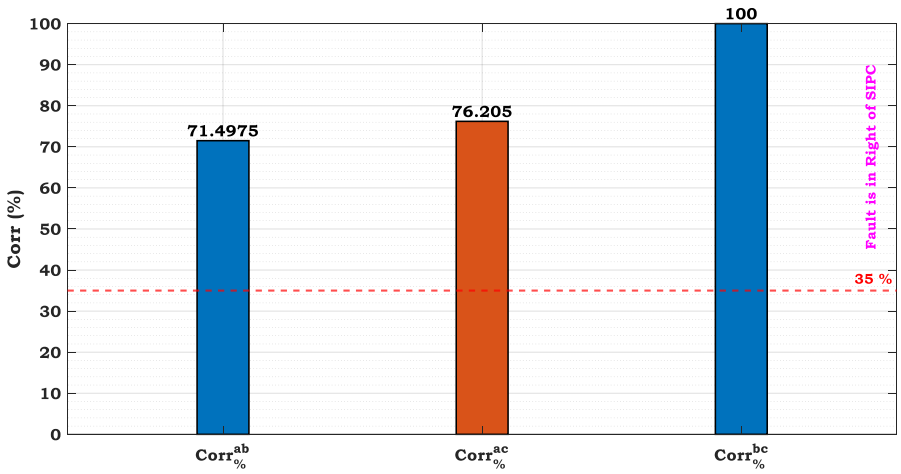


Fig. 40. Faulty segment detection index in Scenario 11.

### 4-2-12 Scenario 12

Scenario 12 assumes a cg fault has occurred at a distance of 185 km from bus S, with a resistance of 100 ohms, at time t = 0.05 seconds. The three-phase current resulting from this fault, measured at bus S, is shown in Fig. 38. Based on the results obtained for the current, the g index for all three phases has been measured for a quarter of a cycle following the fault. According to the results, it is evident that during this time interval, the g values have exceeded zero. These calculated values confirm that a fault has occurred on the transmission line. Next, the correlation coefficients between the two phases—based on the g index—are plotted in Fig. 39. Using the values from this figure, the faulty section detection index is calculated and presented in Fig. 40. As shown, all values exceed the threshold of 0.35, indicating that the fault has occurred between bus R and the SIPC bus.

AUT Journal of Electrical Engineering
10.22060/eej.2025.24075.5651

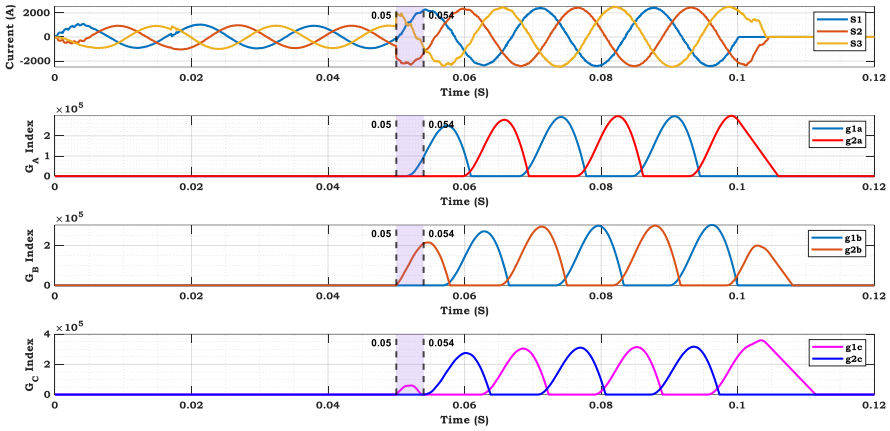


Fig. 41. Three-phase current waveforms and *g* indices in Scenario 12.

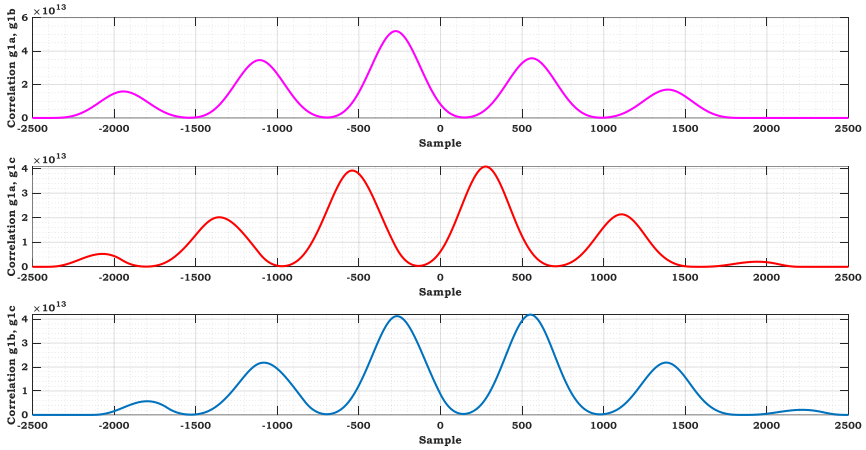


Fig. 42. Correlation index for *g* coefficients in Scenario 12.

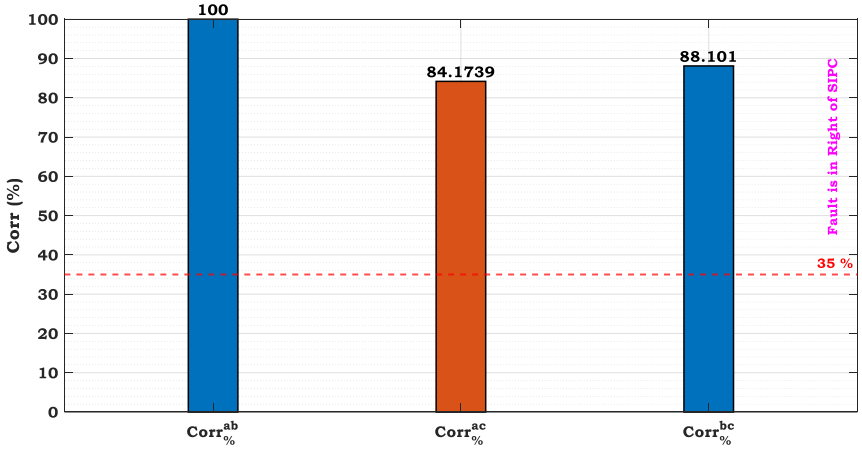


Fig. 43. Faulty segment detection index in Scenario 12.

10.22060/eej.2025.24075.5651

## 5. Sensitivity Analysis of the Proposed Algorithm

In the design and evaluation of protection algorithms, assessing their performance under non-ideal conditions and critical scenarios plays a pivotal role in validating their practical robustness. While many algorithms perform well under normal operating conditions, the presence of disturbances—such as noise, current transformer (CT) saturation, transient phenomena due to switching, and severe loading—can significantly compromise their accuracy and stability. Therefore, conducting a comprehensive sensitivity analysis is a vital step in examining the resilience, adaptability, and reliability of the proposed algorithm against disturbances and nonlinear phenomena. This section presents five representative scenarios designed to evaluate the behavior of the proposed method under challenging conditions. These include a high-impedance fault, noise injection into measurement signals, CT saturation, heavy load switching, and the startup of a three-phase induction motor. Each scenario reflects practical and realistic conditions encountered in power systems, and their analysis provides a deeper understanding of the algorithm's strengths and limitations. The objective of this analysis is to identify the operational limits of the algorithm under extreme conditions, evaluate its precision in detecting fault type and location, and assess its ability to distinguish between actual faults and fault-like transients. Each scenario is independently examined, and the algorithm’s performance is evaluated using behavioral indicators such as response stability, detection accuracy, and disturbance tolerance.

### 5-1- Scenario S1: Sensitivity to High-Impedance Faults

In this scenario, a single-phase-to-ground fault (ag) with very high fault resistance (500 Ω) is applied at a distance of 175 km from bus S at time t = 0.05 s. High-impedance faults (HIFs) are among the most challenging disturbances for protection systems, as they generate low fault currents that may go undetected by conventional relays. Despite the weak fault signal and boundary conditions, the proposed algorithm

successfully identified both the faulted phase and its location. This result, reported in Table (2), Row S1, demonstrates the algorithm's capability to detect weak faults using damping- and dynamic-based indices.

### 5-2- Scenario S2: Sensitivity to Noise Injection in Three-Phase Currents

This scenario evaluates the impact of noise on the algorithm's performance. A phase-to-phase fault (bc) with a resistance of 5 Ω is applied at a distance of 75 km from bus S at t = 0.05 s. Simultaneously, random white noise with a signal-to-noise ratio (SNR) of 20 dB is injected into all three-phase current signals—from one cycle before the fault until breaker operation. Analysis of the results shows that the algorithm accurately detected both the faulted phases and location without any misclassification, confirming its robustness against measurement noise. The critical SNR threshold for performance degradation was estimated to be approximately 36 dB. These results are presented in Table (2), Row S2.

### 5-3- Scenario S3: Sensitivity to CT Saturation

In this scenario, a two-phase-to-ground fault (abg) with a fault resistance of 1 Ω occurs at a distance of 150 km from bus S at t = 0.05 s. The CT saturation phenomenon is modeled based on the specifications of a real industrial current transformer, as cited in reference [34]. The magnetic characteristic of the CT is designed to enter saturation immediately upon fault initiation. The DC component of the output current has a time constant of 50 ms, which represents the algorithm's critical threshold. For time constants below this value, the algorithm correctly detects the fault. The results, shown in Table. 2, Row S3, confirm the algorithm's reliable performance even in the presence of waveform distortion caused by CT saturation.

### 5-4- Scenario S4: Sensitivity to Heavy Load Switching

In this scenario, at t = 0.05 s, a three-phase load rated at 2.5 MW with a power factor of 0.95 is connected to bus R via a fast-switching device. Although no actual fault occurs in the system, the inrush current associated with load switching closely resembles the transient signature of a fault. Nevertheless, the proposed algorithm successfully distinguishes this transient from a genuine fault, preventing any

unnecessary protective actions. The results, reported in Table. 2 , Row S4, highlight the algorithm's precision in discriminating non-fault transients from actual fault events.

### 5-5- Scenario S5: Sensitivity to the Startup of a Three-Phase Induction Motor

In this scenario, a squirrel-cage three-phase induction motor rated at 4 MW, 6.6 kV, and a lagging power factor of 0.8 is connected to bus R through a transformer and circuit breaker. The motor is started at t = 0.05 s, generating an inrush current approximately 6.5 times its rated current, lasting for about 0.2 seconds. This transient closely mimics the profile of a phase-to-ground fault. The proposed algorithm correctly identifies this transient event and refrains from triggering protective commands. The findings, detailed in Table 2, Row S5, confirm the robustness of the algorithm under heavy loading and startup conditions.

Table 2. Sensitivity Analysis Results for Various Test Scenarios of the Proposed Algorithm.

| Scenario | $g_1$ | | | $g_2$ | | | Corr (a, b) % | Corr (a, c) % | Corr (b, c) % | Detecting the occurrence of a fault | Identify the faulty section |
|---|---|---|---|---|---|---|---|---|---|---|---|
| | a | b | c | a | b | c | | | | | |
| **S1** | ✓ | ✗ | ✓ | ✗ | ✓ | ✗ | 100 | 46 | 39 | ✓ | **after SIPC** |
| **S2** | ✗ | ✗ | ✓ | ✗ | ✓ | ✗ | 0.12 | 0.66 | 100 | ✓ | **before SIPC** |
| **S3** | ✓ | ✓ | ✗ | ✓ | ✓ | ✗ | 100 | 56 | 40 | ✓ | **after SIPC** |
| **S4** | ✗ | ✗ | ✗ | ✗ | ✗ | ✗ | 2.35 | 0.09 | 4.36 | ✗ | ---------- |
| **S5** | ✗ | ✗ | ✗ | ✗ | ✗ | ✗ | 8.66 | 5.3 | 2.65 | ✗ | ---------- |

The analysis of results from the five sensitivity scenarios clearly demonstrates that the proposed algorithm exhibits high accuracy, strong discrimination capability, and operational robustness under complex and unstable system conditions. These scenarios, which encompass a combination of realistic and challenging operating environments, can be categorized into two main groups. In the first three scenarios, actual faults occurred in the system under adverse conditions such as high measurement noise, current transformer (CT) saturation, and high fault impedance. In contrast, the final two scenarios involve critical but fault-free events, including heavy load switching and induction motor startup. In both groups, the algorithm exhibited appropriate and differentiated behavior—accurately detecting and localizing faults when present, and successfully avoiding false positives in the absence of actual faults.

10.22060/eej.2025.24075.5651

In scenarios S1 to S3, despite the presence of faults, the system was subjected to significant disturbances such as low fault currents (due to high-impedance faults), measurement noise, and nonlinear CT saturation. Under such conditions, traditional protection schemes often either fail to detect the fault or respond with significant delay. However, the proposed method—relying on the first phase of its structure, namely the CUSUM index—was able to capture persistent statistical deviations in signal behavior and detect the fault in less than a quarter cycle. A key advantage of the CUSUM mechanism is that, unlike methods based on absolute current magnitudes, it is not affected by waveform shape or signal amplitude. It responds only when a structured and sustained deviation pattern is observed. This feature enables the algorithm to detect faults even under weak signal conditions, as in scenario S1, or in the presence of severe waveform distortion, as in scenario S3. In the case of noise (scenario S2), the algorithm's stability in the presence of random disturbances demonstrated that its internal statistical decision-making framework is capable of distinguishing white Gaussian noise from genuine fault signatures.

In the next step, the second phase of the algorithm—based on computing inter-phase correlation coefficients—accurately localized the faulted section in all three scenarios. The structural impact of the SIPC, which divides the line into two electrically asymmetric segments from the relay's perspective, introduces distinguishable correlation patterns among the current signals on either side. By analyzing the time-domain vectors of CUSUM outputs for each phase and calculating pairwise correlation coefficients, the algorithm constructs a decision index that is then compared against a predefined threshold to determine the fault location. The method's ability to maintain this behavior under conditions such as CT saturation or strong noise confirms the stability of its vector-based structure and reflects a deep understanding of the dynamic characteristics of SIPC-equipped systems. In contrast, the final two scenarios (S4 and S5) represent fault-like but benign transients caused by heavy load switching and motor startup. In these cases, the algorithm was expected to remain passive and suppress any false fault indication. As shown in Table 2, the CUSUM indices in these scenarios did not exceed the detection thresholds, and the correlation coefficients did not exhibit any fault-like structure—meaning the algorithm correctly classified these high-

intensity but non-fault events as non-fault conditions. This capability is particularly important, as many protection algorithms are prone to false positives under such disturbances. The proposed method, by effectively distinguishing transient disturbances from true fault patterns, successfully prevents unnecessary protective actions. In summary, the results of the sensitivity analysis confirm that the proposed algorithm—through its two-phase structure combining dynamic CUSUM-based analysis and inter-phase correlation evaluation—demonstrates not only high sensitivity and precision, but also notable resilience and selectivity under realistic operating conditions. Its accurate consideration of the asymmetry introduced by SIPC and its robust multivariate statistical processing make it a reliable and practical solution for real-world protection of SIPC-compensated transmission lines.

## 6. Comparison and Discussion

This section aims to compare the performance of the proposed algorithm in detecting fault occurrence and identifying the faulted segment in transmission lines compensated with SIPC, alongside three well-known methods published within the past year. For this evaluation, the algorithms presented in these three references were implemented and adapted for use in SIPC-compensated transmission lines to detect faults and determine the faulted section. The results of implementing these three methods, as well as the proposed approach, are presented in Table. 3.

Table 3. Results of the Comparison Between the Proposed Method and Previous Studies.

| Reference | Method Title | Required Signals for Implementation | Computational Complexity | Time Required to Extract Results (ms) | Accuracy in 5400 Test Scenarios (%) |
|---|---|---|---|---|---|
| **[14]** | EMD-HT-FD | Three-phase current | High | 50 to 80 | 43 |
| **[23]** | VMD-TEO-FDLS | Three-phase current | Very High | 30 to 40 | 58 |
| **[29]** | ROCO-PSAPD-PAPSII Scheme | Three-phase voltage and current | Very High | 9 to 15 | 66 |
| **Proposed Method** | CUSUM-CORR Scheme | Three-phase current | Very Low | 4 | 98.46 |

According to the results in Table 3 and the in-depth technical analysis of the algorithms proposed in references [14], [23], and [29], it becomes evident that their poor performance in SIPC-compensated transmission lines stems from a fundamental incompatibility with the dynamic, nonlinear, and injection-based behavior of the SIPC architecture. In reference [14], the EMD-HT algorithm decomposes the phase current signal using Empirical Mode Decomposition (EMD), followed by application of the Hilbert Transform (HT) on the dominant IMF to compute instantaneous energy for fault detection. While this method may perform adequately in fixed series capacitor-compensated lines, in SIPC-equipped systems—where each phase includes two independently controlled SSSC units injecting dynamic voltage—the current signal becomes highly non-stationary and multi-component. As a result, EMD suffers from mode-mixing, preventing accurate IMF extraction, and the energy index derived via HT fails to reflect meaningful fault-related features. Moreover, this method is structurally incapable of identifying the faulted segment with respect to the SIPC, which is critical in systems where the compensator splits the line into two distinct electrical zones.In reference [23], although the VMD-TEO approach appears more advanced—using Variational Mode Decomposition and the Teager Energy Operator to extract fault-related energy—it inherently assumes TCSC-type compensation and relies on converging iterative decomposition. In the SIPC environment, however, continuous voltage injection by SSSCs rapidly alters the frequency profile of the current signal, leading to divergence in IMF selection and incorrect identification of the faulted phase. Furthermore, the spectral overlap between injected harmonics and fault-induced components undermines the energy index's reliability, especially for faults occurring near or across the SIPC node.In reference [29], the ROCO-PSAPD-PAPSII scheme uses synchronized PMU data from both line terminals to compute the rate of change of positive sequence active power (ROCO-PSAPD) and the phase angle of the integrated impedance (PAPSII). Although theoretically promising, this approach requires a robust and high-speed communication infrastructure and is highly sensitive to signal distortions. In SIPC-based lines, the voltage/current inversion phenomenon—caused by asymmetric voltage injection from dual SSSCs—can falsely trigger the ROCO-PSAPD index, misclassifying power flow disturbances as faults. Moreover, the PAPSII index, based on impedance angle between terminals, becomes unreliable because the effective line

impedance is dynamically altered by the SSSCs, which are not modeled in the algorithm's formulation. Collectively, these methods—despite their computational complexity—are not equipped to handle the nonlinearity, segmental decoupling, voltage asymmetry, and high-frequency transients intrinsic to SIPC-compensated systems. In contrast, the proposed method in this study leverages a lightweight, model-free statistical approach using only the three-phase current from a single line terminal. It combines the CUSUM algorithm with inter-phase correlation matrix analysis to detect abrupt changes in current behavior and reliably identify the faulted segment relative to the SIPC. Crucially, these indicators respond directly to structural features in the fault-induced current waveform, without reliance on synchronized measurements or frequency-domain decomposition. This makes the algorithm robust against the complexities of SIPC dynamics. As a result, it correctly identified the fault type and location in 5317 out of 5400 scenarios (98.46% accuracy), outperforming the other methods, which achieved only 43%, 58%, and 66% accuracy, respectively. Therefore, both in terms of quantitative performance and algorithmic compatibility with the physical behavior of SIPC-based systems, the proposed method offers a demonstrably superior and practically viable protection solution.

## 7. Conclusion

This paper presented a robust and intelligent algorithm for the detection, classification, and localization of asymmetrical faults in SIPC-compensated transmission lines, with an emphasis on real-time implementation and operational resilience. The proposed method, rooted in a two-phase statistical structure, utilizes the CUSUM technique to detect the onset of disturbances and employs inter-phase correlation analysis to localize the faulted section relative to the SIPC. Unlike traditional methods that rely on threshold-based current magnitudes, this approach demonstrates significant immunity to measurement noise, CT saturation, and high fault impedance, as verified by the sensitivity analysis. The algorithm's structure enables decision-making based on the dynamic behavior and statistical evolution of input current signals, rather than their instantaneous values. This deep statistical insight allows the method to detect subtle deviations in signal patterns with high temporal precision—achieving fault detection in less than a quarter

10.22060/eej.2025.24075.5651

cycle—while effectively filtering out non-fault transients such as motor startups and load switching. The use of $g_1$ and $g_2$ indices derived from phase-wise CUSUM enables accurate detection of fault inception, while the correlation-based decision index ensures correct identification of the faulted section despite the asymmetric topology introduced by the SIPC. The method was validated through comprehensive simulations under 5,400 different fault and system conditions, achieving a remarkable overall accuracy rate of 98.46%. Among these, 12 diverse scenarios were selected for detailed analysis, covering various fault types, fault locations (on both sides of the SIPC), fault resistances, and power flow directions. The algorithm performed successfully across all of them. Furthermore, five dedicated sensitivity analysis scenarios were designed to evaluate the robustness of the algorithm under challenging and realistic conditions. The algorithm proved highly resilient in detecting real faults in the presence of Gaussian noise, CT saturation, and high-impedance fault conditions (S1–S3), and it successfully avoided false detection in non-fault but critical events (S4–S5). This confirms the discriminative capability and operational selectivity of the proposed approach, even in scenarios where many conventional methods fail or produce unreliable responses. Another key strength of the proposed method lies in its adaptability to the physical topology and behavioral dynamics of SIPC devices. By explicitly modeling the asymmetric current distribution around the SIPC and exploiting its influence on the correlation structure of phase currents, the algorithm exhibits a profound contextual awareness that extends beyond conventional relay logic. In summary, the presented approach is not only accurate and fast but also robust, scalable, and practical for real-world deployment in modern power systems with SIPC. Future research may focus on extending the algorithm to identify the faulted phase(s), locate the exact fault point along the line, and integrate it into digital relays or SCADA environments for real-time operation.

10.22060/eej.2025.24075.5651

**Abbreviations**

| | |
|---|---|
| $B_{eq}$ | SIPC equivalent suspensions |
| $B_{eq1}$ | Equivalent suspensions of series 1 converter |
| $B_{eq2}$ | Equivalent suspensions of series 2 converter |
| $Corr^{ab}\%$ | Correlation coefficient between a and b |
| $Corr^{ac}\%$ | Correlation coefficient between a and c |
| $Corr^{bc}\%$ | Correlation coefficient between b and c |
| $E(X)$ | Expected value of X |
| $E(Y)$ | Expected value of Y |
| $g_K(1)$ | The test result of the actual sampled value taken at the kth moment |
| $g_K(2)$ | The test result of symmetrical of the sampled value taken at the kth moment |
| $g_{Ka}$ | The test result of phase a |
| $g_{Kb}$ | The test result of phase b |
| $g_{Kc}$ | The test result of phase c |
| $h$ | Denotes the threshold parameter |
| $I_1$ | Current of line 1 |
| $I_2$ | Current of line 2 |
| $i_{d1}$ | Converter injection current 1 |
| $i_{d2}$ | Converter injection current 2 |
| $jX_1$ | Equivalent reactance of transformer winding 1 |
| $jX_2$ | Equivalent reactance of transformer winding 2 |
| $k$ | Bus number counter |
| $K_1$ | Controller gain |
| $m_2$ | Modulation coefficient of converter 2 |
| $m_2$ | Modulation coefficient of converter 1 |
| $P_0$ | Active power component of the SIPC operating point on the apparent power circle. |
| $P_{inj,r}$ | Active power injected into r |
| $P_{inj,S}$ | Active power injected into S |
| $P_r$ | The active power of the r bus |
| $P_S$ | The active power of the S bus |
| $Q_{inj,r}$ | Reactive power injected into r |
| $Q_{inj,S}$ | Reactive power injected into S |
| $Q_{IPC}$ | IPC reactive power |
| $Q_r$ | The reactive power of the r bus |
| $Q_{REF}$ | Reference reactive power |
| $Q_S$ | The reactive power of the S bus |
| $S_0$ | Apparent power at the SIPC operating point, composed of $P_0$ and $Q_0$. |
| $S_{IPC}$ | IPC apparent power |
| $S_K$ | The sample taken at the *k*th moment |
| $S_K(1)$ | The actual sampled value taken at the kth moment |
| $S_K(2)$ | Symmetrical of the sampled value taken at the kth moment |
| $S_{REF}$ | Reference apparent power |
| $T_1$ | Controller time constant |
| $T_2$ | Transformers 2 |
| $Th1$ | Threshold |
| $v$ | Reference parameter and the output index of the algorithm |
| $V(X)$ | Variance of X |
| $V(Y)$ | Variance of Y |
| $V_d$ | DC link voltage |
| $V_r$ | r bus voltage |

| | |
|---|---|
| $V_S$ | S bus voltage |
| $V_{S1}$ | $V_{S1}$ voltage |
| $V_{S2}$ | $V_{S2}$ voltage |
| $V_{Se1}$ | Series 1 converter voltage |
| $V_{Se2}$ | Series 2 converter voltage |
| $X$ | Random variable |
| $Y$ | Random variable |
| $\alpha_1$ | Angle between voltage $V_{Se1}$ and voltage $V_S$ |
| $\alpha_2$ | Angle between voltage $V_{Se2}$ and voltage $V_S$ |
| $\beta$ | Control angle that sets the active-to-reactive power ratio at the SIPC output. |
| $\delta_{Sr}$ | Change in active power at bus $r$ caused by adjustments of α and β. |
| $\rho$ | Instantaneous radius of the SIPC apparent power vector in the Q–P plane, set by α. |
| $\rho_{max}$ | Maximum attainable radius of SIPC apparent power, limited by design. |
| $\tau$ | Time constant associated with the SIPC control response or transient injection delay. |
| $\varphi_1$ | Angle between voltage $V_{S1}$ and voltage $V_S$ |
| $\varphi_2$ | Angle between voltage $V_{S2}$ and voltage $V_S$ |
| $\varphi_S$ | Angle between voltage VS and zero reference |

## References

[1] M. Abasi, M. Joorabian, A. Saffarian, S.G. Seifossadat, A Comprehensive Review of Various Fault Location Methods for Transmission Lines Compensated by FACTS devices and Series Capacitors, Journal of Operation and Automation in Power Engineering, 9(3) (2021) 213–225.
[2] M. Abasi, M. Joorabian, A. Saffarian, S.G. Seifossadat, A novel complete dynamic and static model of 48-pulse VSC-based GUPFC for parallel transmission lines, International Journal of Industrial Electronics Control and Optimization, 3(4) (2020) 447–457.
[3] J. Pourhossein, G. Gharehpetian, S. Fathi, Static Inter-Phase Power Controller (SIPC) modeling for load flow and short circuit studies, Energy Conversion and Management, 64 (2012) 145–151.
[4] M. Abasi, A. Nahavandi, J. Ebrahimi, G.B. Gharehpetian, Power flow and power quality improvement of a residential-industrial microgrid using 72-pulse inverter-based UIPC, International Journal of Electrical Power & Energy Systems, 164 (2025) 110449.
[5] J. Ebrahimi, M. Abasi, Design of a power management strategy in smart distribution networks with wind turbines and EV charging stations to reduce loss, improve voltage profile, and increase hosting capacity of the network, Journal of Green Energy Research and Innovation, 1(1) (2024) 1–15.
[6] H. Eristi, Fault diagnosis system for series compensated transmission line based on wavelet transform and adaptive neuro-fuzzy inference system, Measurement, 46(1) (2013) 393–401.
[7] A. Verma, A. Yadav, ANN based fault detection & direction estimation scheme for series compensated transmission lines, in: 2015 IEEE international conference on electrical, computer and communication technologies (ICECCT), IEEE, 2015, pp. 1–6.
[8] G. Kapoor, A contemporary discrete wavelet transform based twelve phase series capacitor compensated transmission line protection, Int. J. Engineering Research and Technology, 7(5) (2018) 263–271.
[9] P.K. Mishra, A. Yadav, M. Pazoki, FDOST-based fault classification scheme for fixed series compensated transmission system, IEEE Systems Journal, 13(3) (2019) 3316–3325.
[10] P.K. Mishra, A. Yadav, Combined DFT and fuzzy based faulty phase selection and classification in a series compensated transmission line, Modelling and Simulation in Engineering, 2019(1) (2019) 3467050.
[11] A. Abu-Siada, M.I. Mosaad, S. Mir, Voltage–current technique to identify fault location within long transmission lines, IET Generation, Transmission & Distribution, 14(23) (2020) 5588–5596.

[12] M. Abasi, A. Rohani, F. Hatami, M. Joorabian, G.B. Gharehpetian, Fault location determination in three-terminal transmission lines connected to industrial microgrids without requiring fault classification data and independent of line parameters, International Journal of Electrical Power & Energy Systems, 131 (2021) 107044.
[13] A. Saffarian, M. Abasi, Fault location in series capacitor compensated three-terminal transmission lines based on the analysis of voltage and current phasor equations and asynchronous data transfer, Electric Power Systems Research, 187 (2020) 106457.
[14] O. Koduri, R. Ramachandran, M. SaiVeerraju, EMD-HT Based Fault Detection for Series Capacitor Compensated Line, in: 2025 3rd International Conference on Smart Systems for applications in Electrical Sciences (ICSSES), IEEE, 2025, pp. 1–4.
[15] P. Dash, S. Samantray, Phase selection and fault section identification in thyristor controlled series compensated line using discrete wavelet transform, International Journal of Electrical Power & Energy Systems, 26(9) (2004) 725–732.
[16] S. Samantaray, P. Dash, Pattern recognition based digital relaying for advanced series compensated line, International Journal of Electrical Power & Energy Systems, 30(2) (2008) 102–112.
[17] B.Y. Vyas, R. Maheshwari, B. Das, Improved fault analysis technique for protection of Thyristor controlled series compensated transmission line, International Journal of Electrical Power & Energy Systems, 55 (2014) 321–330.
[18] E. Reyes-Archundia, J.L. Guardado, J. Gutiérrez-Gnecchi, E. Moreno-Goytia, N. Guerrero-Rodriguez, Fault analysis in TCSC-compensated lines using wavelets and a PNN, Neural Computing and Applications, 30(3) (2018) 891–904.
[19] R. Nale, H. Verma, M. Biswal, An enhanced fuzzy rule based protection scheme for TCSC compensated double circuit transmission system, International Journal of Modelling and Simulation, 41(2) (2021) 120–130.
[20] H. Fasihipour, S. Seyedtabaii, Fault detection and faulty phase (s) identification in TCSC compensated transmission lines, IET Generation, Transmission & Distribution, 14(6) (2020) 1042–1050.
[21] S. Biswas, B.K. Panigrahi, P.K. Nayak, G. Pradhan, S. Padmanaban, A single-pole filter-assisted improved protection scheme for the TCSC-compensated transmission line connecting large-scale wind farms, IEEE Journal of Emerging and selected topics in industrial electronics, 5(2) (2023) 346–358.
[22] P.K. Mishra, A. Yadav, Fault classification scheme for TCSC compensated transmission line using MODWPT-BTEC, e-Prime-Advances in Electrical Engineering, Electronics and Energy, 9 (2024) 100729.
[23] S. Nazeer, C. Mahalakshmi, P. Kanta Rao, VMD-TEO for improved fault detection and segment identification in thyristor-controlled series compensation systems, Engineering Research Express, 7(2) (2025) 025360.
[24] A.M. El-Zonkoly, H. Desouki, Wavelet entropy based algorithm for fault detection and classification in FACTS compensated transmission line, International Journal of Electrical Power & Energy Systems, 33(8) (2011) 1368–1374.
[25] Q. Liu, Y.Y. Chang, Y. Xu, Fault Position Identification for Series Compensated Lines with SSSC Based on Improved Wavelet Packet Entropy, Advanced Materials Research, 383 (2012) 5200–5205.
[26] M. Geethanjali, M. Anju Alias, T. Karpaga Senthil Pandy, Discrete wavelet transform based fault detection and classification in a static synchronous series compensated transmission system, in: Proceedings of the Third International Conference on Soft Computing for Problem Solving: SocProS 2013, Volume 1, Springer, 2014, pp. 85–94.
[27] E. Reyes-Archundia, J.L. Guardado, E. Morenogiytia, J.A. Gutierrez-Gnecchi, F. Martinez-Cardenas, Fault detection and localization in transmission lines with a static synchronous series compensator, Advances in Electrical and Computer Engineering, 15(3) (2015) 17–22.
[28] M.M. Almomani, S.F. Algharaibeh, Modelling and testing of a numerical pilot distance relay for compensated transmission lines, International Journal of Scientific Research and Engineering Development, 3(6) (2020) 776–786.

[29] M.M. Elhabashy, H. Sharaf, D.K. Ibrahim, Reliable protection for static synchronous series compensated double-circuit transmission lines based on positive sequence active power calculations using PMUs, Electric Power Systems Research, 223 (2023) 109695.
[30] M. Abasi, M. Razaz, G. Seifossadat, S. Moosapour, Presenting a new formulation to analyze and determine unbalance voltage produced at the place of load resulting from network and loads unbalance and asymmetry of transmission lines in radial power systems, Majlesi Journal of Energy Management, 4(3) (2015) 1–7.
[31] G. Sudha, T. Basavaraju, A comparison between different approaches for fault classification in transmission lines, in: 2007 IET-UK International Conference on Information and Communication Technology in Electrical Sciences (ICTES 2007), IET, 2007, pp. 398–403.
[32] F. Gustafsson, F. Gustafsson, Adaptive filtering and change detection, Wiley New York, 2000.
[33] S. Mohanty, A. Pradhan, A. Routray, A cumulative sum-based fault detector for power system relaying application, IEEE transactions on power delivery, 23(1) (2008) 79–86.
[34] M. Abasi, A. Saffarian, M. Joorabian, S.G. Seifossadat, Fault classification and fault area detection in GUPFC-compensated double-circuit transmission lines based on the analysis of active and reactive powers measured by PMUs, Measurement, 169 (2021) 108499.